

## MULTI-DIMENSIONAL SIMULATIONS OF THE ACCRETION-INDUCED COLLAPSE OF WHITE DWARFS TO NEUTRON STARS

L. DESSART<sup>1</sup>, A. BURROWS<sup>1</sup>, C.D. OTT<sup>2</sup>, E. LIVNE<sup>3</sup>, S.-Y. YOON<sup>4</sup>, N. LANGER<sup>5</sup>

*Draft version February 7, 2020*

### ABSTRACT

We present 2.5D radiation-hydrodynamics simulations of the accretion-induced collapse (AIC) of white dwarfs, starting from 2D rotational equilibrium configurations, thereby accounting consistently for the effects of rotation prior to and after core collapse. We focus our study on 1.46- $M_{\odot}$  and 1.92- $M_{\odot}$  progenitors, with a central density of  $5 \times 10^{10} \text{ g cm}^{-3}$ , and initial rotational to gravitational energy ratios of  $7.6 \times 10^{-3}$  and  $8.3 \times 10^{-2}$ . Efficient electron capture leads to the collapse to nuclear densities of these cores a few tens of milliseconds after the start of the simulations. The shock generated at bounce moves slowly, but steadily, outwards. Within 50–100 ms, the stalled shock breaks out of the white dwarf along the poles. The blast is followed, 200–300 ms after bounce, by a neutrino-driven wind that develops within the excavated white dwarf, in a cone of  $\sim 40^\circ$  opening angle about the pole, with a mass loss rate of  $5\text{--}8 \times 10^{-3} M_{\odot} \text{ s}^{-1}$ . The ejecta have an entropy on the order of  $20\text{--}50 k_B/\text{baryon}$ , and the electron fraction is bimodal, with peaks at 0.25 (due to the neutrino-driven wind) and 0.5 (due to the original blast and the wind along the pole). By the end of the simulations, at  $\gtrsim 600$  ms after bounce, the explosion energy has reached  $3\text{--}4 \times 10^{49} \text{ erg}$  and the outflowing mass has reached a few times  $10^{-3} M_{\odot}$ . We estimate the asymptotic explosion energies to be within a factor of  $\sim 2$  of these values, thus significantly lower than those seen and inferred in the core collapse of massive progenitors. AIC of WDs thus represents one instance where a neutrino mechanism leads undoubtedly to a successful, albeit weak, explosion.

While the total electron-neutrino luminosities are comparable to those observed in core collapse simulations, the effects of rotation are to reduce the “ $\nu_{\mu}$ ” and  $\bar{\nu}_e$  luminosities, the latter by one order of magnitude. Additionally, the neutron stars resulting from such AIC of white dwarfs are strongly aspherical, with neutrinospheres having disk-like shapes, akin to a polar-pinched oblate surface. In the faster rotating (1.92- $M_{\odot}$ ) model, this configuration results in a strong latitudinal dependence of the neutrino flux, enhanced in the polar direction and reduced in the equatorial direction compared to a non-rotating case. Such a latitudinal dependence is reminiscent of that observed and modeled in the winds of fast-rotating oblate luminous stars.

The deleptonized region connected to the neutrinosphere has a butterfly, rather than a spherical shape. Moreover, the neutrino-driven wind originating in the vicinity of the distorted neutrinosphere sees a lower electron-neutrino flux further away from the poles, resulting in a latitudinal dependence of the electron fraction of the ejected material.

In both models, a quasi-Keplerian 0.1–0.5  $M_{\odot}$  disk remains in the equatorial region, that should later be accreted by the neutron star on longer, viscous timescales.

Compared to standard core collapse, our AIC simulations show no perceptible signs of convection associated with the negative lepton radial-gradient in the protoneutron star, no  $l = 1, 2$  oscillations associated with the vortical-acoustic instability, no late time (protoneutron star) core oscillations, and no sizable neutron star kick.

We estimate the gravitational wave emission by aspherical matter motion and anisotropic neutrino emission from our models. We find that gravitational waves from axisymmetric AIC events may be detected by current and future LIGO-class detectors from anywhere in the Milky Way.

*Subject headings:* hydrodynamics – neutrinos – rotation – stars: neutron – stars: supernovae: general – stars: white dwarfs

### 1. INTRODUCTION

<sup>1</sup> Department of Astronomy and Steward Observatory, The University of Arizona, Tucson, AZ 85721; luc@as.arizona.edu, burrows@as.arizona.edu

<sup>2</sup> Max-Planck-Institut für Gravitationsphysik, Albert-Einstein-Institut, Golm/Potsdam, Germany; cott@aei.mpg.de

<sup>3</sup> Racah Institute of Physics, The Hebrew University, Jerusalem, Israel; eli@frodo.fiz.huji.ac.il

<sup>4</sup> Astronomical Institute “Anton Pannekoek”, University of Amsterdam, Kruislaan 403, 1098 SJ, Amsterdam, The Netherlands; scyoon@science.uva.nl

<sup>5</sup> Astronomical Institute, Utrecht University, Princetonplein 5, 3584 CC, Utrecht, The Netherlands; n.langer@astro.uu.nl

Stars can follow a few special evolutionary routes to form an unstable Chandrasekhar mass core. A main-sequence star of more than  $\sim 8 M_{\odot}$  evolves to form either a degenerate O/Ne/Mg core (Barkat et al. 1974; Nomoto 1984, 1987; Miyaaji & Nomoto 1987) or a degenerate Fe core (Woosley & Weaver 1995), which, due to photodisintegration of heavy nuclei and/or electron capture, collapses to form a protoneutron star (PNS). If an explosion ensues, the event is associated with a Type II supernovae (SN). Less massive stars end their lives as white dwarfs. White dwarfs located in a binary system may accrete from a companion and achieve the Chan-

drasekhar mass, triggering the thermonuclear runaway of the object and leading, it is supposed, to Type Ia SN, leaving no remnant behind.

However, a third class of objects is expected. Theoretically, massive white dwarfs with O/Ne/Mg cores, due to their high central density ( $\gtrsim 10^{10} \text{ g cm}^{-3}$ ), experience rapid electron capture that leads to the collapse of the core. This is accretion-induced collapse (AIC), an alternative path to stellar disruption through explosive burning, currently associated with Type Ia SN (Nomoto & Kondo 1991). Various paths may lead to a white dwarf with such properties. One possibility is the coalescence of two white dwarfs (Mochkovitch & Livio 1989), with either C/O or O/Ne/Mg cores, although few such binary systems have yet been observed with a cumulative mass above the Chandrasekhar mass. There is still uncertainty as to whether such binary systems would not undergo thermonuclear runaway rather than collapse. Since the coalescence of two white dwarfs requires a shrinking of the orbit through gravitational radiation, these systems will take many gigayears to coalesce. An alternative formation mechanism is via single-degenerate systems, through a combination of high original white dwarf mass and mass and angular-momentum accretion by mass transfer from a (non-degenerate) H/He star (Nomoto & Kondo 1991). Binary star population synthesis codes predict the occurrence of the AIC of white dwarfs with a galactic rate of  $8 \times 10^{-7} \text{ yr}^{-1}$  to  $8 \times 10^{-5} \text{ yr}^{-1}$ , depending, amongst other things, on the treatment of the common-envelope phase and mass transfer (Yungelson & Livio 1998). The set of parameters leading to a Type Ia rate of  $10^{-3} \text{ yr}^{-1}$  corresponds to an AIC rate of  $5 \times 10^{-5} \text{ yr}^{-1}$ . The observed Type Ia rate of  $\sim 3 \times 10^{-3} \text{ yr}^{-1}$  (Madau et al. 1998; Blanc et al. 2004; Manucci et al. 2005) would imply a galactic AIC rate of  $1.5 \times 10^{-4} \text{ yr}^{-1}$ . These rates are likely functions of galaxy and metallicity (Yungelson & Livio 2000; Belczynski et al. 2005; Greggio 2005; Scannapieco & Bildsten 2005). Based on r-process nucleosynthetic yields obtained from previous simulations of the AIC of white dwarfs, Fryer et al. (1999) inferred rates ranging from  $\sim 10^{-5}$  to  $\sim 10^{-8} \text{ yr}^{-1}$ . Overall, AICs are not expected to occur more than once per 20–50 standard Type Ia events; because they are intrinsically rarer, they remain to be identified and observed in Nature.

Whatever their origin, their fundamental nature is to accrete both mass and angular momentum from a companion object. Rotation is, therefore, a key physical property. Prior to core collapse, differential rotation acts as a stabilizing agent for shell burning by widening its spatial extent through enhanced mixing and reducing the envelope density through centrifugal support (Yoon & Langer 2004). Mass accretion also leads to an increase of the central density, which may rise up to a few  $10^{10} \text{ g cm}^{-3}$ , establishing suitable conditions for efficient electron capture on Mg/Ne nuclei. By the time of core collapse and depending on the evolutionary path followed, such white dwarfs may cover a range of masses from  $\gtrsim 1.35 M_{\odot}$  up to  $\sim 2 M_{\odot}$  ( $2.7 M_{\odot}$ ) in the case of a non-degenerate (degenerate) companion, potentially well in excess of the standard Chandrasekhar limit, and possessing an initial rotational energy up to  $\sim 10\%$  of their gravitational binding energies. At such values, the centrifugal potential leads to a deformation of the white dwarf from spherical symmetry, equipotentials and iso-

pressure surfaces adopting a peanut-like shape in cross section for the largest rotation rates. Such structures are obtained in the 2D differentially rotating equilibrium white dwarf models constructed by Yoon & Langer (2005, YL05; see also Liu & Lindblom 2001).

In the past, the collapse of O/Ne/Mg cores originating from stars in the  $8\text{--}10 M_{\odot}$  range has been studied in 1D by Baron et al. (1987ab), Mayle & Wilson (1988), and Woosley & Baron (1992), who showed that the shock generated at core bounce stalls rather than leading to a prompt explosion. However, Hillebrandt et al. (1984) and Mayle & Wilson (1988) obtained delayed explosions, the former after 20–30 ms, and the latter after  $\sim 200$  ms, supposedly driven by neutrino energy deposition behind the stalled shock. Woosley & Baron (1992) found the emergence of a sustained neutrino-driven wind, with a mass loss rate of  $0.005 M_{\odot} \text{ s}^{-1}$  and with an ejecta electron fraction of the order of 0.45, showing promise, modulo uncertainties, for a contribution to the enrichment of the ISM in r-process elements. Using 1D/2D SPH simulations, Fryer et al. (1999) reproduced the simulations of Woosley & Baron (1992), confirmed that the shock stalls due to the copious neutrino losses associated with core bounce, did not find prompt explosion, and, depending on the equation of state (EOS) employed, observed a delayed explosion. They focused mostly on the early phase, prior to the neutrino-driven wind, and found an ejected mass of low- $Y_e$  material of  $\sim 0.05 M_{\odot}$ , depending on adopted model assumptions. Their 2D simulations with solid-body rotation showed similar properties to their 1D equivalents, the authors attributing the small differences to the different grid resolution. This may partly stem from the essentially spherical explosion triggered just  $\lesssim 100$  ms after core bounce, ejecting the fast-rotating material in the outer mantle. Consequently, at the end of their 2D simulations, they obtain very slow rotation rates for the PNS, i.e., of  $\sim 1$  s. Recently, Kitaura et al. (2005) re-inspected the collapse of the progenitor model used by Hillebrandt et al. (1984). They confirmed again the by-now well-accepted idea that no prompt explosion occurs, but instead obtain a successful, though sub-energetic, delayed explosion in spherical symmetry, powered by neutrino heating and a neutrino-driven wind that sets in  $\sim 200$  ms after bounce.

A primary motivation for this work is to improve upon these former investigations that assumed one-dimensionality, sphericity, and/or zero-rotation, and start instead from the more physically-consistent 2D models of YL05, thereby fully accounting for the effects of rotation on the collapse, bounce, and post-bounce evolution of the white dwarf core and envelope, as well as for the strong asphericity of the progenitor. Our study uses VULCAN/2D (Livne et al. 2004; Walder et al. 2005) to perform 2D Multi-Group Flux Limited Diffusion (MGFLD) radiation hydrodynamics simulations. As we will demonstrate, rotation plays a major role in the post-bounce evolution, making 1D investigations of such objects of limited utility. By carrying out the simulations from  $\sim 30$  ms before bounce to  $\gtrsim 600$  ms after bounce, we capture a wide range of physical processes, including the establishment of a strong, fast, and aspherical neutrino-driven wind. We model the centrifugally-supported equatorial regions and the large angular momentum budget leading to the formation of

a sizable accretion disk. Moreover, our Eulerian investigation is better-suited than previous Lagrangean studies to explore the neutrino-driven wind that develops after  $\gtrsim 200$  ms. Finally, despite the relative scarcity of AIC in Nature, these simulations represent interesting examples for the formation of disks around neutron stars.

The main findings of this work are the following: We find that the AIC of white dwarfs forms  $\sim 1.4 M_{\odot}$  neutron stars, expelling a modest mass of a few  $10^{-3} M_{\odot}$  mostly through a neutrino-driven wind that develops  $\gtrsim 200$  ms after bounce, and that they lead to very modest explosion energies of  $5\text{--}10 \times 10^{49}$  erg. Accounting for the rotation and the asphericity of the progenitor white dwarfs reveals a wealth of phenomena completely absent in former investigations. The shock wave generated at core bounce emerges through the poles rather than the equator, and it is in this excavated polar region that the neutrino-driven wind develops. The strong asphericity of the newly-formed protoneutron stars leads to a latitudinally-dependent neutrino flux, while the effects of rotation modify the relative flux magnitude of different neutrino flavors. Besides mass accretion by both the neutron star and mass ejection by the initial blast and the subsequent wind, we find a sizable component that survives and resides in a quasi-Keplerian disk, which obstructs the wind flow at low latitudes. This disk will be accreted by the neutron star only on longer, viscous timescales.

In the next two sections, we present the two selected progenitor models in more detail; we also discuss the radiation-hydrodynamics code VULCAN/2D and the various assumptions made. In §4, we present the simulation results, focusing on the general temporal evolution from the start until  $\gtrsim 600$  ms, a time by which the neutrino-driven wind has reached a steady state. We then analyse in more detail the various components of these simulations. In §5, we discuss the properties of the nascent neutron stars, with special attention paid to the geometry of the neutrinospheres. In §6, we discuss the neutrino signatures, both in terms of luminosity and energy distribution. In §7, we focus on the residual material lying at low latitudes, forming a quasi-Keplerian disk. In §8, we turn to the energetics of the explosion and describe in detail the main component of the simulations at late times, i.e., the neutrino-driven wind. In §9, we analyse the electron fraction of the ejected material and address the relevance of the AIC of white dwarfs for neutron-rich element pollution of the interstellar medium. In §10, we present the gravitational-wave signal predicted for the AIC of our white dwarf models. In §11, we wrap up with a discussion of the main results of this investigation and present our conclusions.

## 2. INITIAL MODELS

In this section, we present the properties of the AIC progenitors selected in our study and summarize the presentation in §2 of YL05.

The general assumption for the construction of 2D progenitor models for the AIC of white dwarf (YL05) is that the resulting structure of the object is essentially independent of its evolutionary history, the only factors that matter being the given (final) mass, angular momentum, and central density,  $\rho_c$ . Additionally, the angular velocity distribution  $\Omega(r, z)$ , where  $r$  is the cylindrical radius

and  $z$  is the distance to the equator, is determined self-consistently, given a number of properties identified in 1D models: 1) the role played by the dynamical shear instability, 2) the compression (and spin up) of the surface layers due to mass accretion which puts its peak angular velocity interior to the surface radius, 3) the adopted surface rotational velocity value (its fraction of the local Keplerian value), and 4) the geometry of the angular velocity profile, which we assume to be constant on cylinders, i.e.,  $\Omega = \Omega(r)$ . Together with the pressure/density dependence  $P = P(\rho)$ , such rotating stars are called barotropic. Note that the criterion used in YL05 for the shear rate for the onset of the dynamical shear instability is determined using the EOS of Blinnikov et al. (1996).

The 2D rotating models then correspond to equilibrium configurations iteratively found from trial density and angular velocity distributions, using the Self-Consistent-Field method (Ostriker & Mark 1968; Hachisu 1986), under the constraint that the density  $\rho$  is solely a function of the effective potential  $\Psi(r, z)$ , given as the sum of the gravitational potential, i.e.,

$$\Phi(r, z) = -G \int \frac{\rho(r', z')}{|\mathbf{R} - \mathbf{R}'|} d^3 R',$$

and the centrifugal potential, i.e.,

$$\Theta(r) = - \int \Omega^2(r') r' dr',$$

where  $R' = \sqrt{r'^2 + z'^2}$  (Tassoul 2000, YL05).

In this paper, we select two progenitors with masses of  $1.46 M_{\odot}$  and  $1.92 M_{\odot}$  and present their global characteristics in Table 1. Both models have an initial central density  $\rho_c$  equal to  $5 \times 10^{10} \text{ g cm}^{-3}$ . The  $1.46 M_{\odot}$  model serves as a reference for an object with a moderate initial rotational energy  $T$  relative to gravitational energy  $|W|$ , i.e.,  $T/|W| = 0.0076$ , and, indeed, shows only a modest initial departure from spherical symmetry, with a polar ( $R_p$ ) to equatorial ( $R_{eq}$ ) radius ratio  $R_p/R_{eq} = 0.7$ . At the other end of the white dwarf mass spectrum, the  $1.92 M_{\odot}$  model has considerable rotational energy, with initial  $T/|W| = 0.0833$ , and the morphology of the star departs strongly from spherical symmetry, with  $R_p/R_{eq} = 0.28$ . For later reference, we also provide in Table 1 the ratio  $T/|W|$  at the end of the simulations. In practice, the infall of the ambient material causes numerical difficulties soon after the start of the simulation. These difficulties were resolved by trimming the outer and low-density layers of both white dwarf progenitors. While the polar radius is hardly affected, the equatorial radius is reduced to 980 km (down from 1130 km) for the  $1.46 M_{\odot}$  model and 1860 km (down from 2350 km) for the  $1.92 M_{\odot}$  model. The progenitor mass is, however, reduced by less than one part in  $10^6$ . Hence, we do not expect any perceptible effect on the results.

## 3. VULCAN/2D SIMULATION CODE

The simulations discussed in this paper were performed with the Newtonian hydrodynamic code VULCAN/2D (Livne 1993), supplemented with an algorithm for neutrino transport as described in Livne et al. (2004) and Walder et al. (2005). The version of the code used here is the same as that discussed in Dessart et al. (2005)

TABLE 1  
PROPERTIES OF SELECTED AIC PROGENITORS

M $M_{\odot}$	$R_p$ km	$R_{eq}$ km	$J$ erg·s ( $10^{50}$ )	$T$ erg ( $10^{50}$ )	$ W $ erg ( $10^{50}$ )	$T/ W $ initial	$T/ W $ final
1.46	800	1130	0.160	0.7	91.97	0.0076	0.059
1.92	660	2350	1.092	10.57	126.9	0.0833	0.262

and Burrows et al. (2005), and uses the 2D Multi-Group Flux-Limited Diffusion (MGFLD) method to handle neutrino transport (see Appendix A of Dessart et al. 2005). The MGFLD variant of VULCAN/2D is much faster than the more accurate, but considerably more costly multi-angle  $S_n$  variant. Doppler velocity-dependent terms are not included in the transport, although advection terms are. Frequency redistribution due to the subdominant process of neutrino-electron scattering is neglected. Our calculations include 16 energy groups logarithmically distributed in energy from 2.5 to 220 MeV, take into account the electron and anti-electron neutrinos, and bundle the four additional neutrino and anti-neutrino flavors into a “ $\nu_{\mu}$ ” component.

VULCAN/2D uses a hybrid grid, switching from Cartesian in the inner 20 km to spherical-polar further out. In preliminary investigations, we adopted a grid covering 180° about the rotation axis coincident with the  $z$  coordinate. However, we realised that in our AIC simulations nearly perfect top-bottom symmetry was maintained. Hence, only the 1.46- $M_{\odot}$  model was mapped onto a 180° wedge, covering both hemispheres about the equatorial plane, while for the 1.92- $M_{\odot}$ , we limited the computational domain to just one hemisphere. Information on potential neutron star kicks is thus not available for this latter model, but the upshot is that we could run the model with a higher spatial resolution. To summarize, the 1.46- $M_{\odot}$  model uses a grid with a maximum resolution in the Cartesian inner region of 0.56 km, and a minimum resolution of 150 km at a maximum radius of 5000 km, with 121 regularly spaced angular zones to cover 180°. The 1.92- $M_{\odot}$  model uses a grid with a maximum resolution in the Cartesian inner region of 0.48 km, and a minimum resolution of 100 km at a maximum radius of 4000 km, with 71 regularly-spaced angular zones covering 90°.

A tricky part of the set up was to choose the properties of the “ambient” medium surrounding the AIC model. This need arises because our inputs are Lagrangean in spirit, while VULCAN/2D employs a Eulerian grid. Ideally, one would like to have material that merely occupies the space that will soon, after bounce, be replaced by the ejected material following the explosion. A key requirement is, thus, that this material have a very low pressure, to influence as little as possible the properties of the blast, but to allow for a smooth transition from circumstellar to ejected material in a given region of the Eulerian grid. To achieve this, we extended our SHEN EOS (Shen et al. 1998) down to very low densities ( $10 \text{ g cm}^{-3}$ ) and low temperatures ( $10^8 \text{ K}$ ), conditions in which the medium is actually radiation-dominated and, thus, has a pressure that depends mostly on temperature. A suc-

cessful choice was to adopt a density of  $1000 \text{ g cm}^{-3}$  and a temperature of  $4 \times 10^8 \text{ K}$  for the ambient medium surrounding both white dwarf models.

A major deficiency of the white dwarf progenitor models used here is their unknown initial thermal structure, which YL05 did not provide. Given the additional difficulty in handling low temperatures and high densities, we resorted to using a parameterized function of the local density, i.e.,

$$T(r, z) = T_c(\rho_c/\rho(r, z))^{0.35},$$

with  $T_c = 10^{10} \text{ K}$  for the  $1.46-M_{\odot}$  model, and  $T_c = 1.3 \times 10^{10} \text{ K}$  for the  $1.92-M_{\odot}$  model. Note that, similarly, Woosley & Baron (1992) were forced to set a central temperature of  $1.2 \times 10^{10} \text{ K}$  at the start of their simulation.

Figure 1 recapitulates the basic properties of the white dwarf progenitors (left column:  $1.46-M_{\odot}$  model; right column:  $1.92-M_{\odot}$  model) as mapped onto our Eulerian grid. In the top panel, we show a color map of the density on which we superpose line contours of the effective potential  $\Psi$  (defined above), as computed by VULCAN/2D. Our computation of the gravitational potential is based on a multipole expansion in spherical harmonics up to  $l = 33$ . We reproduce the fundamental property of these fast-rotating white dwarf progenitors, in that the isopressure surfaces and the equipotentials coincide. In the bottom panel, we plot the initial angular velocity field. To avoid the distortion of streamlines of the infalling ambient material, the angular velocity is set to zero outside the WD progenitor. Note how, from zero, the angular velocity rises to a maximum value near the outer equatorial radius in the  $1.46-M_{\odot}$  model (left column), while it is much higher in the center of the white dwarf in the  $1.92-M_{\odot}$  model (right column). As we will show below, rotation has a much bigger impact on the collapse phase for the latter configuration. We also overplot line contours of the temperature for each model, following the prescription outlined in the above paragraph.

Finally, we adopt an initial electron fraction of 0.5; the high initial central density permits fast electron capture which soon decreases the  $Y_e$  in the core, leading to bounce on a timescale ten times shorter than typically experienced in the collapse of the core of massive star progenitors (Woosley & Weaver 1995; Heger et al. 2000; Woosley et al. 2002).

#### 4. SIMULATION RESULTS

In this section, we discuss the general properties of the pre- and post-collapse phases for both models at the same time, making comparisons when interesting. We follow the post-bounce evolution of the  $1.46-M_{\odot}$  ( $1.92-M_{\odot}$ ) model for 550 ms (780 ms), for a total of 520 000 (820 000) timesteps.

In Figs. 2–3, we provide entropy (saturated at  $20 \text{ k}_B/\text{baryon}$ , where  $\text{k}_B$  is Boltzmann’s constant) color maps showing the key events in the evolution of both white dwarf models, with starting conditions discussed in the previous section and displayed in Fig. 1. We complement these figures with Fig. 4 for the electron fraction evolution at three reference times (left column:  $1.46-M_{\odot}$  model; right column:  $1.92-M_{\odot}$  model). Note also that we overplot most figures with black arrows representing velocity vectors, whose maximum length is set to 10% of the width (or the height) of the image. The

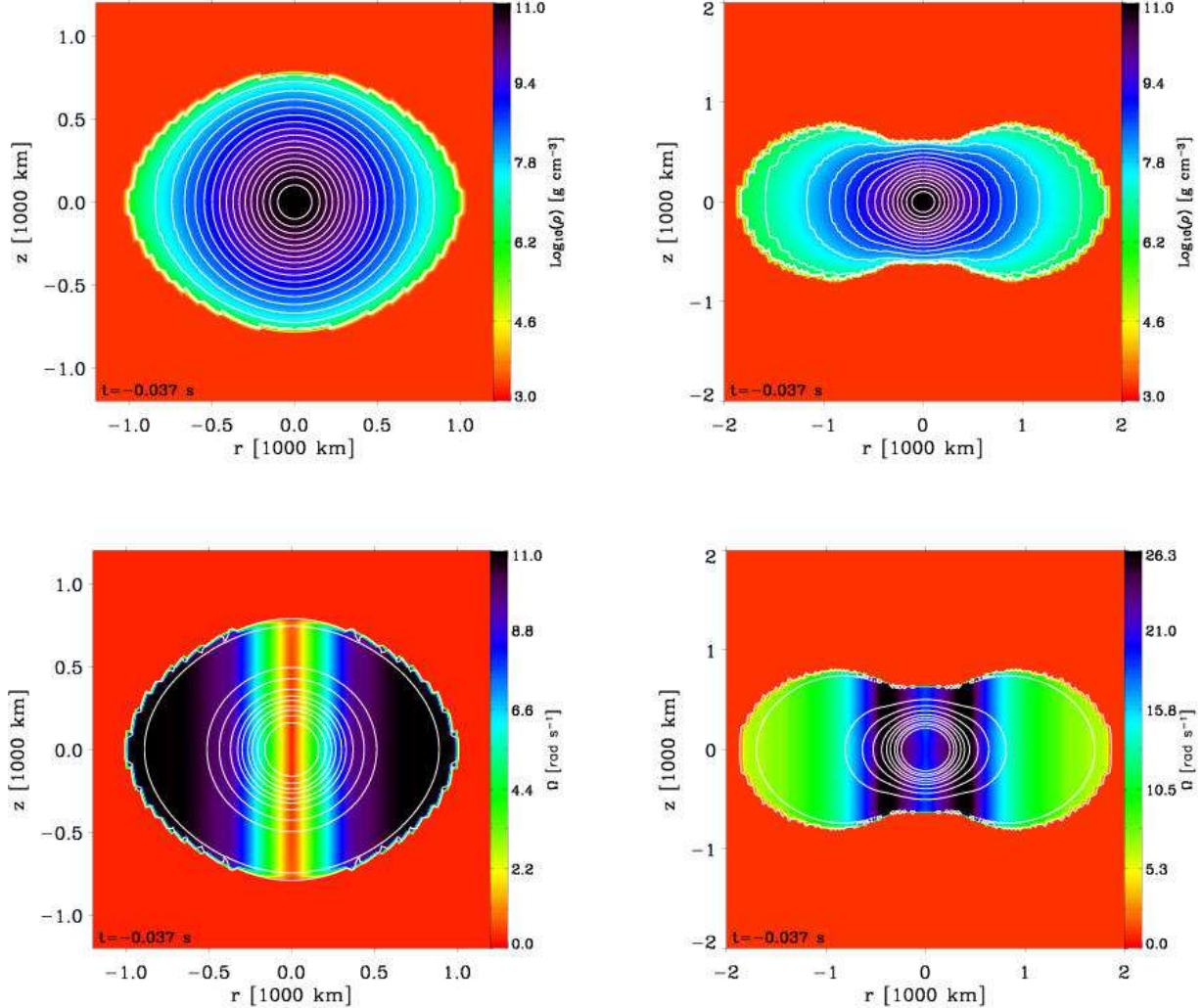


FIG. 1.— *Top:* Color map of the density,  $\rho(r, z)$  (log-scale), at the start of the simulations for the  $1.46\text{-M}_\odot$  model (left) and  $1.92\text{-M}_\odot$  model (right). We overplot the equipotentials corresponding to this equilibrium configuration, whereby the density  $\rho(r, z)$  is solely a function of the effective potential  $\Psi(r, z)$  given as the sum of the gravitational potential, i.e.,  $\Phi(r, z) = -G \int \frac{\rho(r, z)}{|\mathbf{R} - \mathbf{R}'|} d^3 R'$ , and the centrifugal potential, i.e.,  $\Theta(r) = -\int \Omega^2(r') r' dr'$  (see text and YL05 for details). *Bottom:* Same as above, but this time for the angular velocity,  $\Omega(r, z)$ . We overplot contours of the temperature  $T(r, z)$ , chosen to follow the relation  $T(r, z) = T_c(\rho_c/\rho(r, z))^{0.35}$ , where  $T_c = 10^{10}$  K ( $T_c = 1.3 \times 10^{10}$  K) for the  $1.46\text{-M}_\odot$  ( $1.92\text{-M}_\odot$ ) model. Both models have an initial central density  $\rho_c$  equal to  $5 \times 10^{10} \text{ g cm}^{-3}$ . Contours shown are linearly distributed between  $4 \times 10^8$  K and  $10^{10}$  K.

corresponding maximum velocity is then given for each image in the figure captions - we also mention if we saturate the vector lengths. Having a large central density of  $5 \times 10^{10} \text{ g cm}^{-3}$ , both models achieve nuclear densities after the same time of  $\sim 37$  ms. Differences in the bounce properties are attributable to the initial inner angular velocity distributions (Fig. 1). Compared to the  $1.46\text{-M}_\odot$  model, the faster rotator has a lower maximum density at bounce (slightly shifted from the grid center to  $r \sim 1$  km), i.e., 2.2 instead of  $3.1 \times 10^{14} \text{ g cm}^{-3}$ . It manifests an oblate, rather than a spherical, inner region (the inner tens of kilometers) of low entropy ( $\sim 1 k_B/\text{baryon}$ ; visible in red). The deleptonized material in this inner region is, however, aspherically distributed in both models, although more so in the  $1.92\text{-M}_\odot$  model, with the lower  $Y_e$  material lying in a disk structure along the equatorial direction. The flatter density gradient in this direction

and the longer dwell time near the neutrinosphere conspire to produce this enhanced deleptonization. At core bounce, the low-density outer parts of the white dwarf progenitor have not yet started to infall and the progenitor still retains its original shape. The collapse of the inner regions, however, creates a rarefaction wave that triggers the infall of the outer material, with a magnitude that is more pronounced along the poles due to the compact structure of the white dwarf in these directions.

Although we do not observe a prompt explosion (i.e. occurring on a dynamical timescale of just a few milliseconds), the shock progresses slowly outwards without conspicuously stalling. This is slightly different from the core-collapse simulations recently published, whereby the shock *systematically* stalls (Burrows et al. 2005; Buras et al. 2005ab). In the equatorial direction, facilitated by the centrifugal support of the infalling material, the

shock progresses outwards steadily, and is faster in the faster rotating model, reaching a few hundred kilometers after  $\sim 100$  ms. Given the initial constant rotation rate on cylinders (see §2), the *radial* inflow of mass brings angular momentum to the equatorial ( $z \sim 0$ ) region, which becomes more strongly supported, facilitating further the progress of the shock at low latitudes. This exacerbates the non-spherical development of the shock structure in both models. In its wake, we see a few large-scale whirls, resulting from the generation, at mid-latitudes and due to shock passage, of large vortical motions.

In the polar direction, centrifugal support is absent, but the stalling of the shock is prevented by the quickly decreasing accretion rate established by the steeper density gradient, reduced polar radius, and smaller mass budget. Hence, although the shock slowly migrates along the equatorial regions, it soon traverses the surface layer of the white dwarf along the poles and escapes outwards into the ambient medium. Due to the strong asphericity of the progenitor, this occurs only 70 ms after core bounce in the  $1.92\text{-M}_\odot$  model,  $\sim 30$  ms earlier than for the  $1.46\text{-M}_\odot$  model. The ambient medium is then swept up by this blast, whose opening angle is constrained by that of the uncollapsed disk of the progenitor. The outflow expansion rate is larger 30–40 degrees away from the poles than right along the pole, coinciding in Fig. 4 with the lower  $Y_e$  material. The effect is large for the  $1.92\text{-M}_\odot$  model, giving a butterfly shape in cross section to the faster expanding portions of the outflow. Off-axis material has more rotational kinetic energy available to convert to 2D planar ( $r, z$ ) kinetic energy as it streams outward, reducing its rotational velocity while preserving angular momentum, thereby resulting in an enhanced acceleration compared to that of the material situated along the poles and lacking rotational energy.

As the shock expands, it wraps around the disk, typically with a speed near that of the local sound speed. Nearer the pole, the outflow sweeps along the pole-facing side of the pole-excavated white dwarf, entraining surface material and effectively loading the outflow with more mass, causing unsteady fallback onto the neutron star. For the  $1.46\text{-M}_\odot$  progenitor, the shock completely wraps around the low-latitude regions of the white dwarf, and finally emerges from the outer equatorial regions, as witnessed by an outward-moving entropy jump. By 250 ms after bounce, the shock reaches a few thousand kilometers, assumes a near spherical shape, and the entire white dwarf material outside the newly-formed neutron star flows nearly radially outward. In the high-rotation ( $1.92\text{-M}_\odot$ ) progenitor, the white dwarf possesses a lot more mass at near zero-latitude and this confines more drastically the emerging shock along the poles. As the shock migrates outwards, it opens up; it does wrap around the progenitor, but much later than when the shock escapes in the polar directions. Despite the reduced ram pressure associated with centrifugal support, the shock stalls a few hundred milliseconds after bounce along all near-equatorial directions.

Within 100–200 ms, the newly-formed neutron star has a mass of  $\sim 1.4\text{ M}_\odot$ , similar in both models despite the  $0.5\text{ M}_\odot$  difference in progenitor mass. Note that the large neutron star asphericity and the sizably lower density at the neutrinosphere for near-zero latitudes makes this mass definition ambiguous at such early times, es-

pecially in the  $1.92\text{-M}_\odot$  model. Indeed, the neutron star is not clearly distinguishable from the surrounding equatorial material, so imposing either a density cut of  $10^{10\text{--}11}\text{ g cm}^{-3}$  or a radius cut in defining the newly-born neutron star appears arbitrary when determining the residual mass. In the  $1.46\text{-M}_\odot$  model, about  $0.06\text{ M}_\odot$  remains outside of the neutron star, mostly in the equatorial disk region; in the  $1.92\text{-M}_\odot$  model,  $0.6\text{ M}_\odot$  is now lying in this disk-like structure. The rest of the initial mass is outflowing material, which, if selected according to an outward radial velocity discriminant of  $10000\text{ km s}^{-1}$  (comparable to the escape velocity at 3000 km), reaches  $4 \times 10^{-3}\text{ M}_\odot$  for the  $1.46\text{-M}_\odot$  model and  $3 \times 10^{-3}\text{ M}_\odot$  for the  $1.92\text{-M}_\odot$  model. These various components are documented in more detail in §§7–9.

The late-time evolution of both models is characterized by a strong neutrino-driven wind that sets in about 300 ms after bounce, replenishing the grid with denser material (on average  $10^4\text{ g cm}^{-3}$ ) and large velocities (with a maximum of  $30000\text{ km s}^{-1}$  along the poles). The properties of the neutrino-driven wind are very angle-dependent, the density changing by 30% between the pole and the  $40^\circ$  latitude, while the radial outflow velocity varies by a factor of 3 in the  $1.92\text{-M}_\odot$  model. The latitudinal dependence of the mass flux per unit solid angle is therefore dominated by a variation in asymptotic velocity. We will discuss this result in more detail in §8. By the time we stop the simulations, at 550 ms and 780 ms for the  $1.46\text{-M}_\odot$  and  $1.92\text{-M}_\odot$  models, all the ambient medium originally placed around the white dwarf progenitor has been swept away by the neutrino-driven wind, which occupies all the space outside the neutron star and the disk. The electron fraction of the material ejected in the original blast is close to 0.45–0.5, while subsequently, in the neutrino-driven wind, the values are lower, with a pronounced decrease towards lower latitudes (note, however, the high  $Y_e$  right along the pole; see §9).

In Fig. 5, we recapitulate for both models the evolution described above by showing equatorial and polar slices of the density as a function of time. Striking features are the distinct polar and equatorial surface radii, the fast infall of the inner regions to nuclear densities, the slow plowing of the shock along the equatorial directions, superseded in radial extent and velocity by the shock in the polar direction as the surface mass shells collapse in, and finally the emergence of a sequence of density kinks associated with the birth of the fast neutrino-driven wind that sweeps away the previously shocked material that did not leave the grid. Similarly, in Fig. 6, we show slices of the radial velocity,  $V_R$ , along the polar (top row) and equatorial (bottom row) directions for the  $1.46\text{-M}_\odot$  (left column) and  $1.92\text{-M}_\odot$  (right column) models. Notice the much larger infall velocities, similar along the poles and the equator for the  $1.46\text{-M}_\odot$  model, but with a strong latitudinal dependence in the  $1.92\text{-M}_\odot$  model. In that model, the speed contrast between the polar and equatorial directions is  $\sim 30000\text{ km s}^{-1}$ . Overall, the evolution is more rapid along the poles than on the equator, with larger asymptotic velocities ( $30000\text{ km s}^{-1}$  compared with  $10000\text{ km s}^{-1}$ ), and with the establishment of a quasi-stationary outflow at late times along the pole. These radial slices offer a means of better interpreting the fluid velocities, depicted with

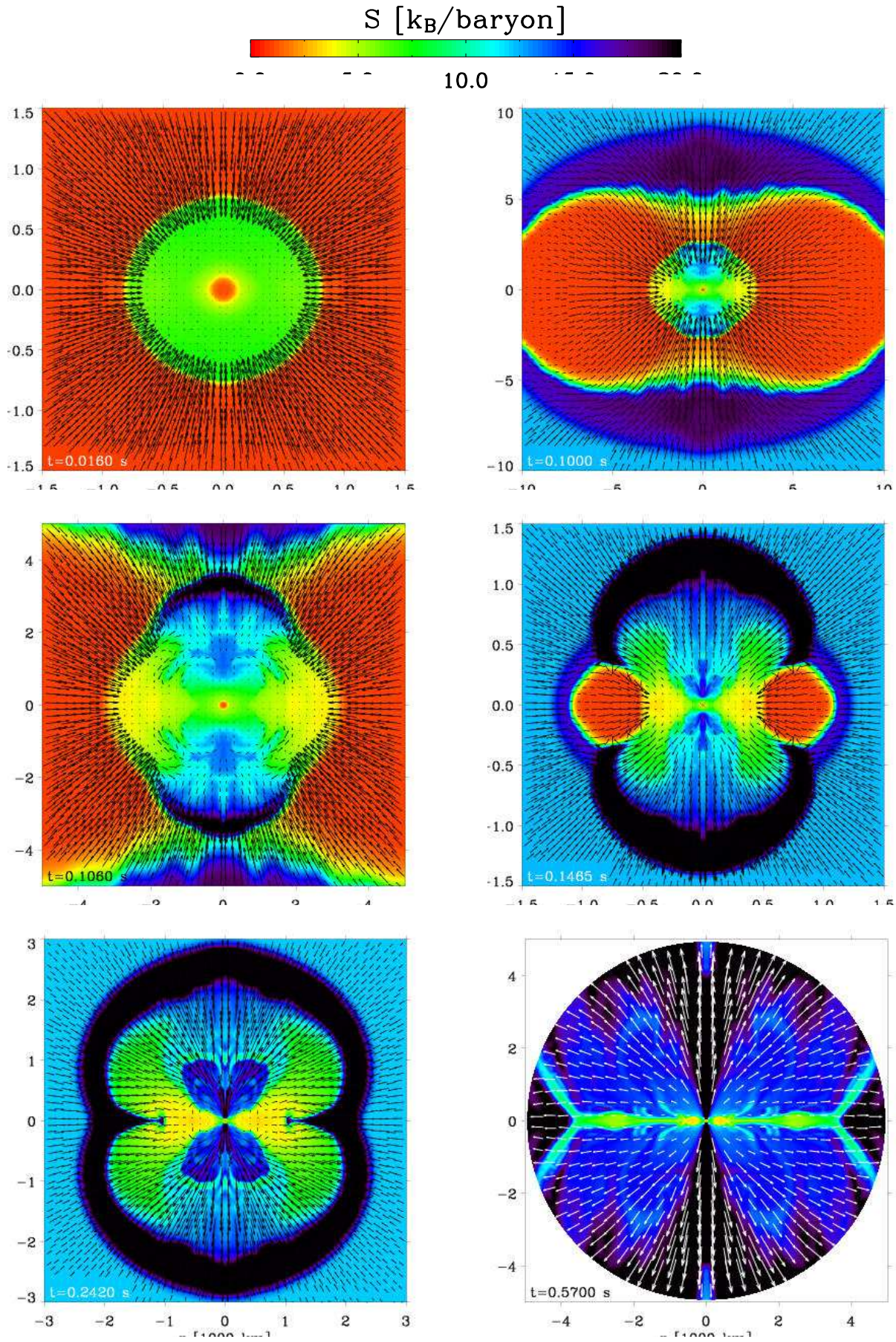


FIG. 2.— Slide sequence of color maps of the entropy covering the post-bounce evolution of the  $1.46 M_{\odot}$  progenitor, with velocity vectors overplotted as black or white arrows. The entropy, reaching up to  $50 k_B$ /baryon at later times, has been saturated at  $20 k_B$ /baryon in all panels to enhance the contrast. From top to bottom, left to right, the vector of maximum length corresponds to a velocity magnitude of  $52500 \text{ km s}^{-1}$ (infall),  $28500 \text{ km s}^{-1}$ (infall),  $24000 \text{ km s}^{-1}$ (infall),  $20500 \text{ km s}^{-1}$ (outflow),  $16500 \text{ km s}^{-1}$ (outflow), and  $34000 \text{ km s}^{-1}$ (outflow). We indicate the time after bounce in the bottom-left corner of each panel. Note also that the spatial scale varies between panels, with widths in the range 300 km to 10000 km. See text for details.

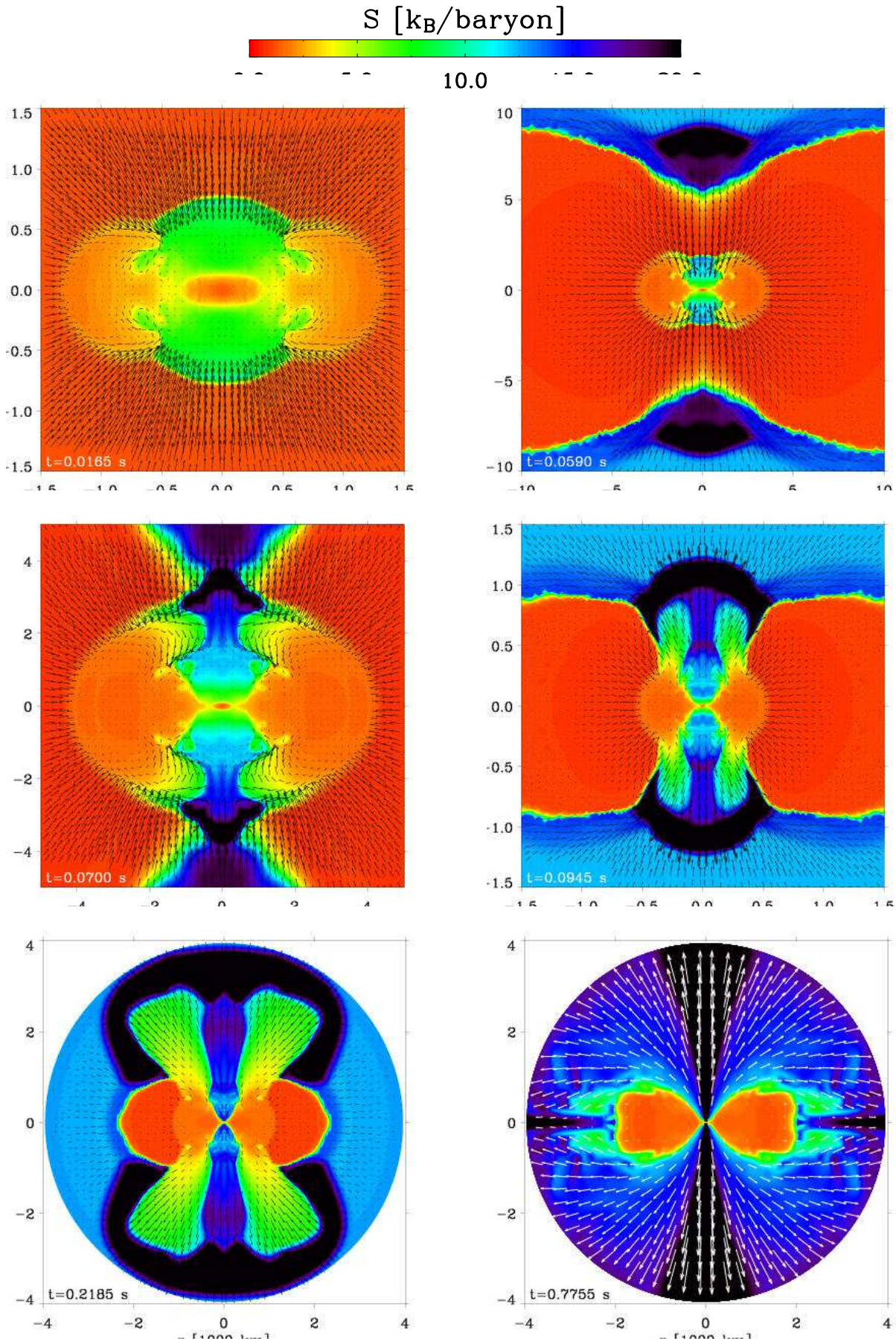


FIG. 3.— Slide sequence of color maps of the entropy covering the post-bounce evolution of the  $1.92 M_{\odot}$  progenitor, with velocity vectors overplotted as black or white arrows. The entropy, reaching up to  $50 k_B$ /baryon at late times, has been saturated at  $20 k_B$ /baryon to enhance the contrast. From top to bottom, left to right, the vector of maximum length corresponds to a velocity magnitude of  $53000 \text{ km s}^{-1}$ (infall),  $36500 \text{ km s}^{-1}$ (infall),  $29000 \text{ km s}^{-1}$ (infall),  $32000 \text{ km s}^{-1}$ (outflow),  $32500 \text{ km s}^{-1}$ (outflow), and  $34500 \text{ km s}^{-1}$ (outflow). We indicate the time after bounce in the bottom-left corner of each panel. Note also that the spatial scale varies between panels, with widths in the range 300 km to 8000 km. See text for details.

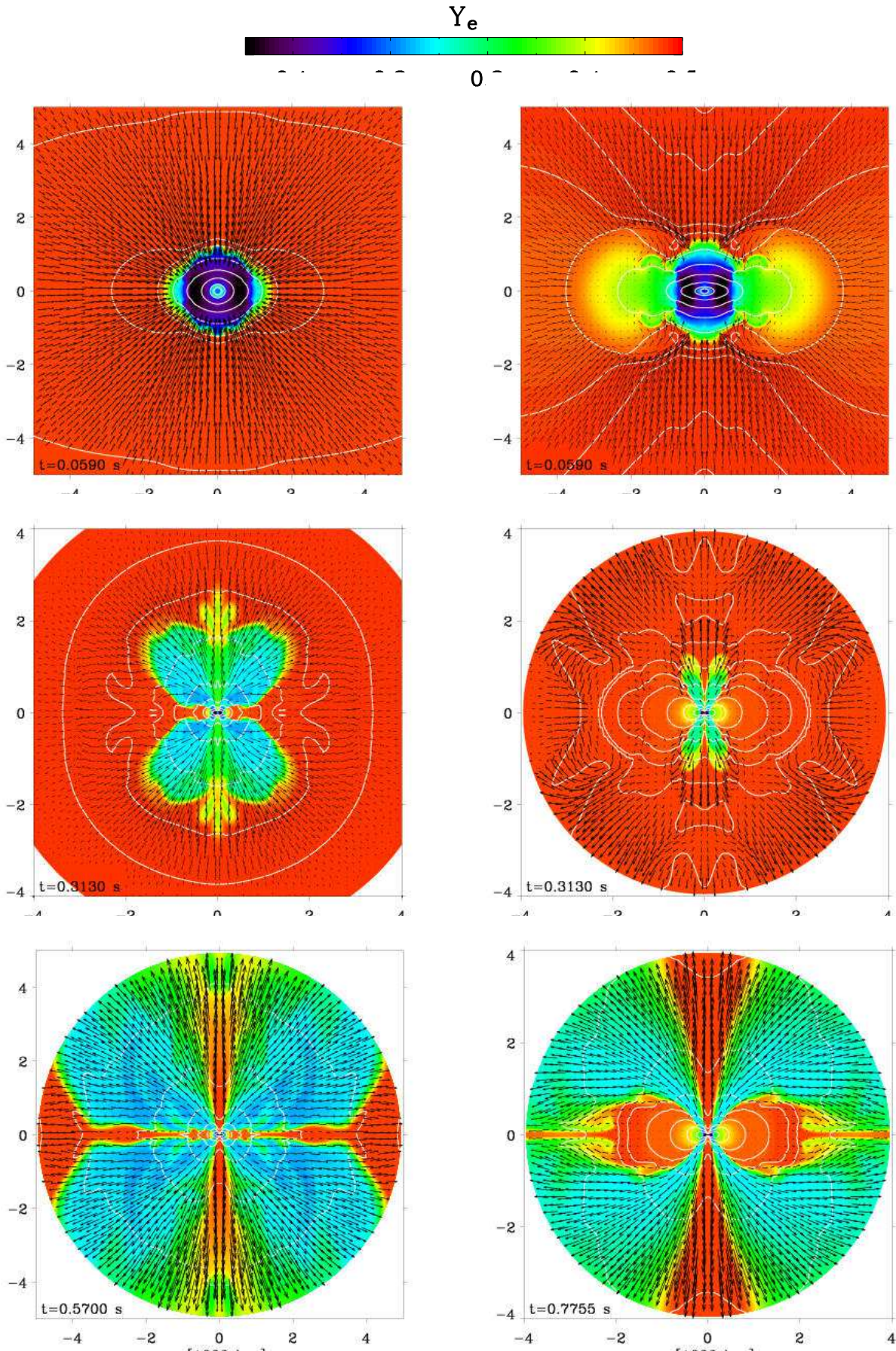


FIG. 4.— Slide sequence of color maps of the electron fraction,  $Y_e$ , covering the post-bounce evolution of the  $1.46\text{-M}_\odot$  (left column) and  $1.92\text{-M}_\odot$  (right column) progenitors, overplotted with velocity vectors, as black arrows. We also superpose isodensity contours as white lines, spaced every decade, starting at  $10^{14}\text{ g cm}^{-3}$  (top row) or  $10^{10}\text{ g cm}^{-3}$  (bottom two rows). From top to bottom, left to right, the vector of maximum length corresponds to a velocity magnitude of  $43500\text{ km s}^{-1}$  (infall),  $36500\text{ km s}^{-1}$  (infall),  $25500\text{ km s}^{-1}$  (outflow),  $19500\text{ km s}^{-1}$  (outflow),  $34000\text{ km s}^{-1}$  (outflow), and  $34500\text{ km s}^{-1}$  (outflow). We indicate the time after bounce in the bottom-left corner of each panel. The spatial scale varies between panels, with widths in the range 500 km to 10000 km (8000 km) for the  $1.46\text{-M}_\odot$  ( $1.92\text{-M}_\odot$ ) model. See text for details.

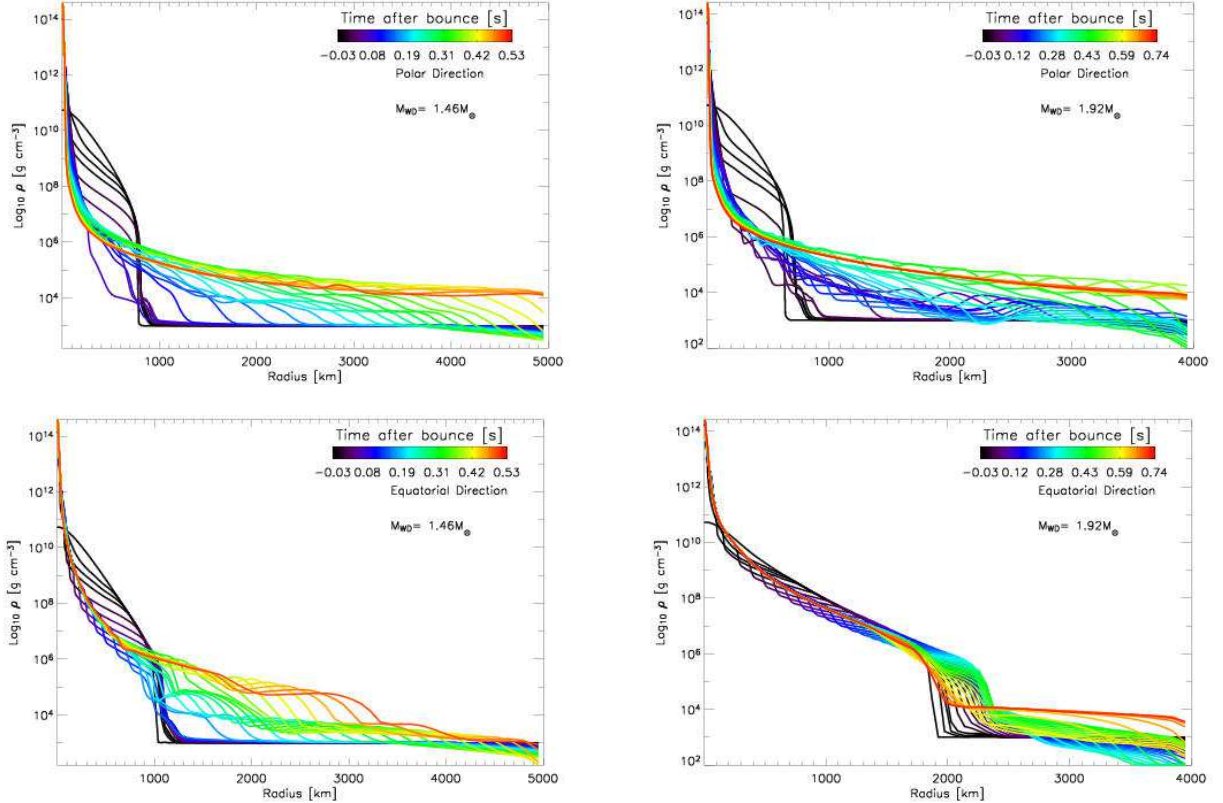


FIG. 5.— *Top:* Time evolution of the polar density profile for the  $1.46 M_{\odot}$  (left column) and  $1.92 M_{\odot}$  (right column) progenitor models. *Bottom:* Same as above, but for the equatorial direction. Note the steeper density profiles at all times along the pole compared to the equatorial direction, highlighting the contrast between the wind (polar direction) and disk (equatorial direction; within a 2000 km radius at 770 ms for the  $1.92 M_{\odot}$  model). See text for discussion.

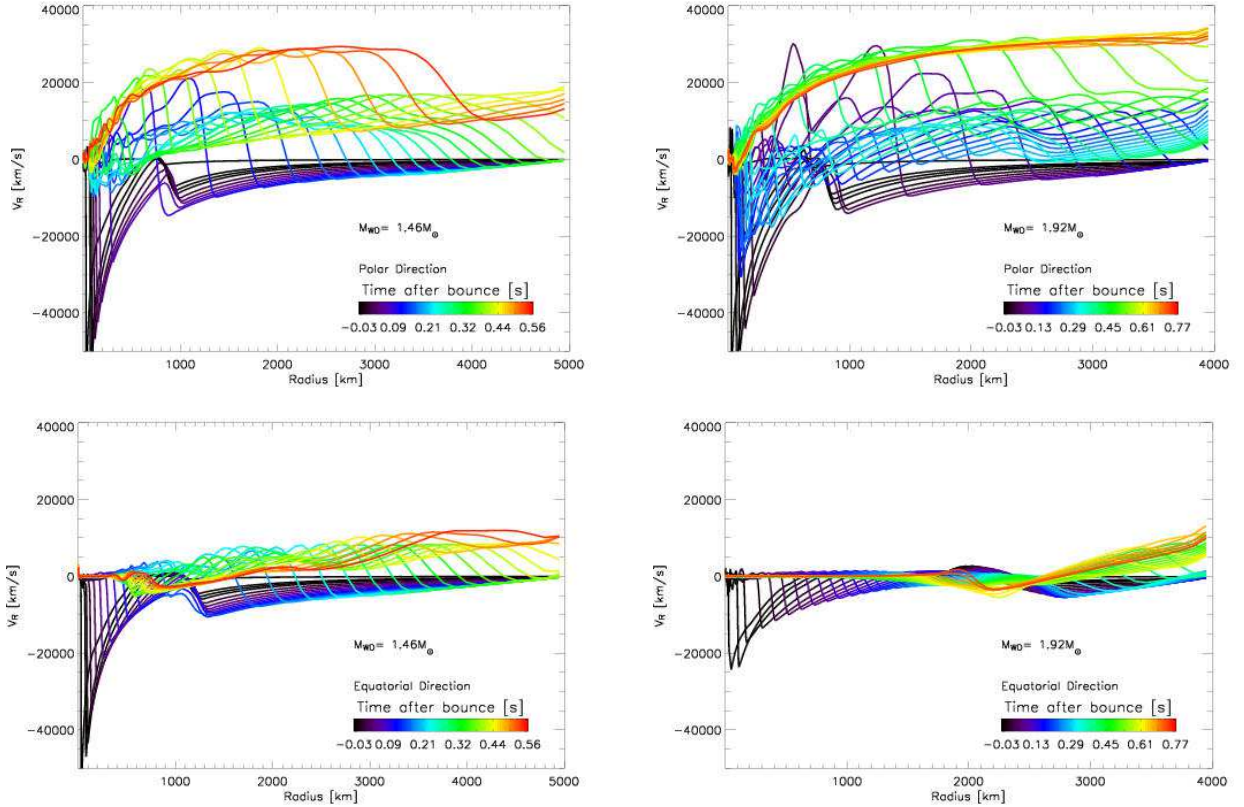


FIG. 6.— Same as for Fig. 5, but this time for the radial velocity  $V_R$ . Note the large contrast between the polar and equatorial pre-bounce (infall) velocities for the  $1.92M_\odot$  model, the fast neutrino-driven wind at late times along the poles, overtaking the slower expansion of the shock generated at core bounce. Along the equator, material shows slow ( $1.46M_\odot$  model) or absent (within a 2000 km radius,  $1.92M_\odot$  model) expansion, belonging to a quasi-Keplerian disk (§7). See text for discussion.

vectors, in most color maps shown in this paper. We also show isodensity contours in most color maps to provide some feeling for the density distribution.

Having described the general properties of the two simulations of the AIC of a  $1.46M_\odot$  and  $1.92M_\odot$  white dwarf, we now address more specific issues, covering the properties of the nascent neutron star (§5), the neutrino signatures (§6), the properties of the residual disk and the angular momentum history (§7), the neutrino-driven wind and the global energetics (§8), the electron fraction of the ejected material (§9), and, finally, the gravitational wave signatures (§10).

## 5. NEUTRON STAR PROPERTIES

The white dwarf progenitors discussed in this paper, due to their evolution to high central densities, high rotational kinetic energies, and high mass, are distinctive in that their cores collapse to form neutron stars rather than being disrupted by the explosive burning of carbon and oxygen.

We find that neutron stars formed from the AIC of the progenitor white dwarfs used in this work are very aspherical (see, for example, Walder et al. 2005; Liu & Lindblom 2001; Janka & Mönchmeyer 1989ab), although there are significant differences in evolution after bounce between the two models. In Fig. 7, we show color maps of the density field 59 ms after bounce (top row), as well as for the last time computed ( $t = 570$  ms after bounce; bottom row) in the  $1.46M_\odot$  model. To render more striking

the level of asphericity of the neutron star “surface,” we overplot the neutrinospheres  $R_\nu(\varepsilon_\nu, r, z)$ , adopting the definition

$$\tau(R_\nu(\varepsilon_\nu, r, z)) = \int_{R_\nu(\varepsilon_\nu, r, z)}^{\infty} \kappa_\nu(\rho, T, Y_e) \rho(r', z') dR' = 2/3,$$

where  $\kappa_\nu(\rho, T, Y_e)$  is the combined material absorption and scattering opacity to neutrinos, and the integration is carried out along radial rays, with  $R' = \sqrt{r'^2 + z'^2}$ , using 30 equally spaced latitudinal directions per quadrant. Strictly, this definition is most appropriate for the photosphere/neutrinosphere in a plane-parallel atmosphere, but it gives a sense of the asphericity of the collapsed core. Note that the above expression contains a dependence both on the neutrino flavor and the neutrino energy  $\varepsilon_\nu$ . In the left column of Fig. 7, line contours correspond to such neutrinosphere radii as a function of energy group, bracketing the peak of the neutrino energy distribution at the neutrinosphere, i.e., between 2.5 and 46 MeV. Material opacity to neutrinos increases with the square of the energy, so that higher-energy neutrinos have larger neutrinospheres. Here, for the  $1.46M_\odot$  model, these radii vary from  $\sim 30$  to  $\sim 120$  km along the equatorial direction, with little departure from sphericity (30% lower values are obtained in the polar direction). In the right panel, line contours correspond to the neutrinosphere for the three different flavors at a neutrino energy ( $\varepsilon_\nu$ ) of 12.5 MeV, associated with the peak of the energy distribution. Note that this is ap-

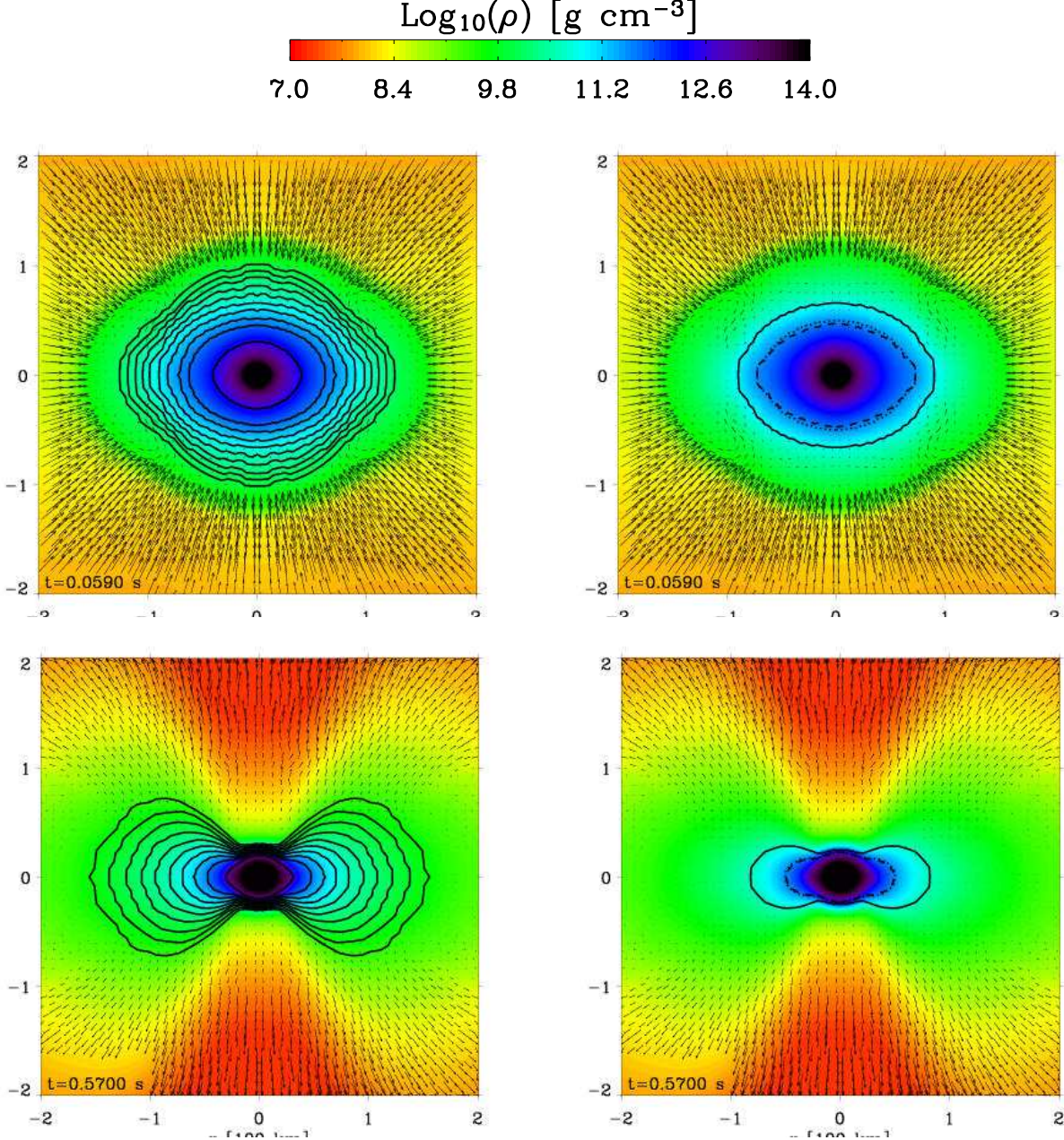


FIG. 7.— *Top:* Color map of the density at 59 ms after bounce for the  $1.46\text{-M}_\odot$  model. *Left:* Neutrinosphere radii for the  $\nu_e$  neutrino for ten energy groups around the peak of the emergent energy distribution, i.e., at 2.5, 5.5, 7.5, 9.5, 12.5, 16, 21, 27, 36, and 46 MeV. *Right:* Neutrinosphere radii at 12.5 MeV for the three neutrino flavors:  $\nu_e$  (solid lines),  $\bar{\nu}_e$  (dotted line), and  $\nu_\mu$  (dash-dotted line, which overlaps with the dotted line). *Bottom:* Same as above, but for the last computed time at 570 ms after bounce. The vector with the maximum length corresponds to a velocity magnitude of  $46300 \text{ km s}^{-1}$  (infall; top panels) and  $9440 \text{ km s}^{-1}$  (outflow; bottom panels). The fixed spatial coverage of the display is  $200 \times 200 \text{ km}^2$ .

proximate, since the neutrino energy distribution hardens with time and manifests a latitudinal dependence (see §6). As in standard 1D and 2D core-collapse computations, we find that the electron neutrinos decouple from matter at larger radii than the  $\bar{\nu}_e$  and  $\nu_\mu$  neutrinos. Here, the former decouple at 90 km (60 km) along the equator (pole), the latter two nearly overlapping and situated inwards at 70 km (50 km). The neutrinospheres show a similar shape for all three flavors (and all energy groups), reflecting the corresponding asphericity in the density field.

In the bottom-row panels, we reproduce the above for the last time in the  $1.46\text{-M}_\odot$  simulation. The departure from sphericity is now considerable, with both an oblateness and a strong pinching of the neutrinospheres along the polar directions. Along the equatorial direction, the radial spacing between neutrinospheres of consecutive and higher energy groups has increased, and the lower (higher) energy groups decouple further in (out) than in the previous snapshot, with neutrinospheres between 20 and 150 km (from 2.5 to 50 MeV), 80 and 50 km (for the  $\nu_e$  neutrino, and  $\bar{\nu}_e$ 、“ $\nu_\mu$ ” neutrinos, respectively). Along

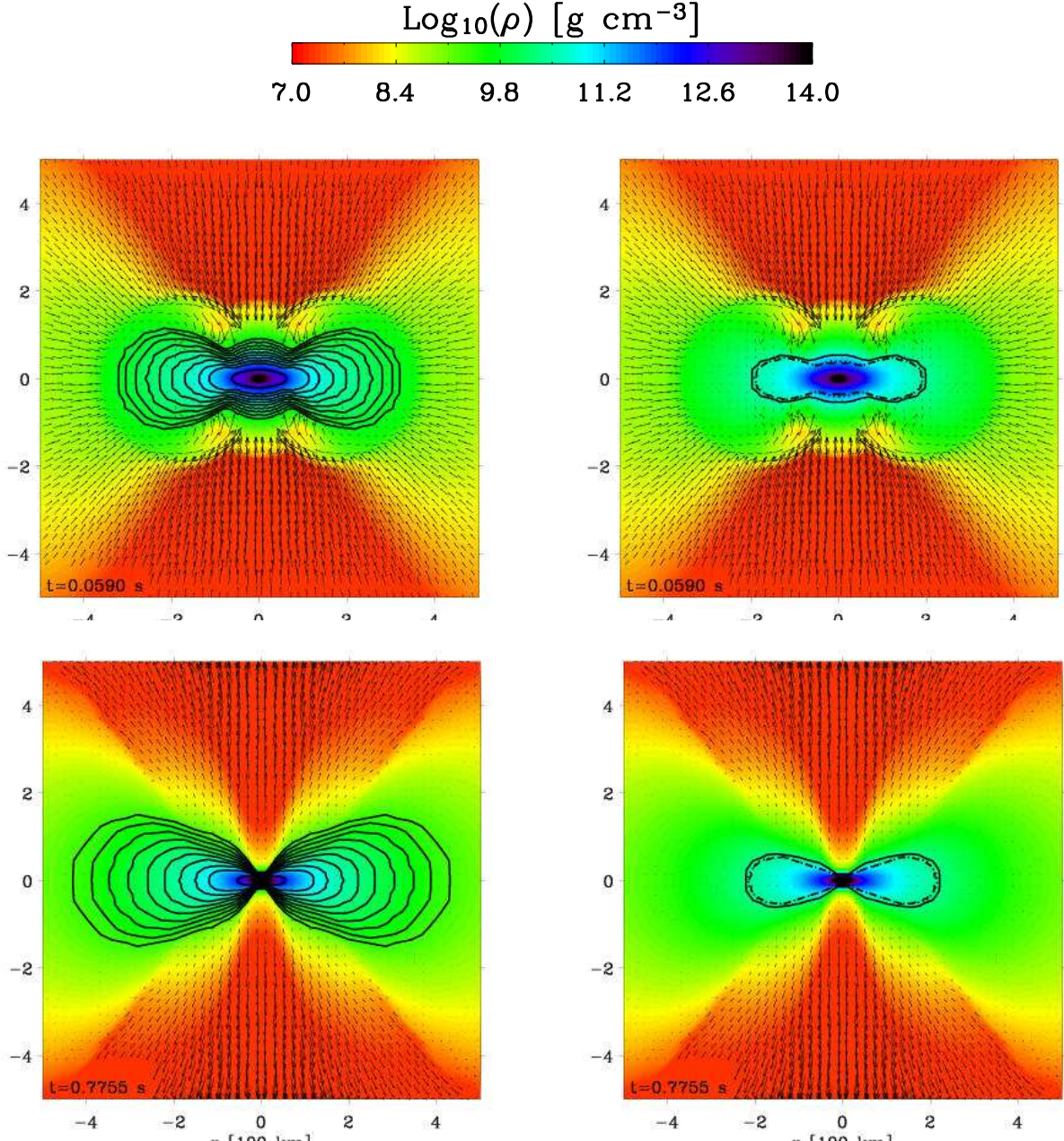


FIG. 8.— *Top:* Color map of the density at 59 ms after bounce for the  $1.92\text{-M}_\odot$  model. *Left:* Neutrinosphere radii for the  $\nu_e$  neutrino for ten energy groups around the peak of the emergent energy distribution, i.e., at 2.5, 5.5, 7.5, 9.5, 12.5, 16, 21, 27, 36, and 46 MeV. *Right:* Neutrinosphere radii at 12.5 MeV for the three neutrino flavors:  $\nu_e$  (solid lines),  $\bar{\nu}_e$  (dotted line), and “ $\nu_\mu$ ” (dash-dotted line, which overlaps with the dotted line). *Bottom:* Same as above, but for the last computed time at 775.5 ms after bounce. The vector of maximum length corresponds to a velocity magnitude of  $36500 \text{ km s}^{-1}$  (infall; top panels) and  $15500 \text{ km s}^{-1}$  (outflow; bottom panels). The fixed spatial coverage of the display is  $500 \times 500 \text{ km}^2$ .

the polar direction, neutrinospheres of all neutrino energy groups (and all neutrino flavors at 12.5 MeV) shown reside in a narrow range of radii between 20 and 30 km (22 to 25 km). Here again, the neutrinospheres depicted follow very closely the contours of density, which is the primary factor controlling the neutrino optical depth.

In Fig. 8, we duplicate Fig. 7 (note the different spatial scale) for the  $1.92\text{-M}_\odot$  model, showing the same quantities both early after bounce (59 ms) and significantly

later at 775.5 ms after bounce. There are numerous differences with the  $1.46\text{-M}_\odot$  model. First, the neutrinospheres are aspherical even right after bounce (top row), with equatorial (polar) radii larger (smaller) by a factor of 2-3 compared with those in the  $1.46\text{-M}_\odot$  model. All flavors reveal similar neutrinosphere locations.

In the  $1.46\text{-M}_\odot$  model, the later ratio of the equatorial and polar radii is 2.5:1, irrespective of energy group and flavor. This becomes 15:1 in the  $1.92\text{-M}_\odot$  model, and is

thus a considerable departure from sphericity; the faster rotating model has a neutrinosphere radius of just 14 km along the pole, but 215 km along the equator. This is the most conspicuous difference with the essentially spherical neutron stars seen in non-rotating simulations of the more standard core collapse of massive stars (Keil et al. 1996; Swesty & Myra 2005; Buras et al. 2005a; Dessart et al. 2005), with neutrinosphere radii of the order of 20–30 km at comparable times after core bounce.

The very aspherical neutron stars formed through the AIC of a white dwarf make the determination of the neutron star mass somewhat ambiguous. Rather than taking the enclosed mass within a given spherical radius, we compute the total mass from all regions above a given mass density. For a density cut of  $10^{10} \text{ g cm}^{-3}$ , we obtain neutron star masses of  $1.42 M_{\odot}$  for the  $1.46-M_{\odot}$  model, and  $1.5 M_{\odot}$  for the  $1.92-M_{\odot}$  model. However, if we adopt a density cut of  $10^{11} \text{ g cm}^{-3}$ , the neutron star masses are, respectively,  $1.39 M_{\odot}$  and  $1.30 M_{\odot}$ . The higher-mass progenitor model has now a smaller neutron star mass, reflecting the strong asphericity of the density field. While we might associate the neutrinosphere with the neutron star surface and with a standard mass density of  $10^{11} \text{ g cm}^{-3}$ , such an association in the present fast rotating neutron star is inappropriate, since the neutrinospheres extend well into regions where the density is  $\lesssim 10^{10} \text{ g cm}^{-3}$ . These neutron star mass values are reached at 100 ms after core bounce and remain essentially constant. The neutrino-driven wind that appears after a few 100 ms decreases the neutron star mass at a rate of just a few  $10^{-3} M_{\odot} \text{ s}^{-1}$  (see §8). Note also that the enhanced centrifugal support in the faster-rotating, higher-mass model leads to bounce at a 30% lower maximum density compared with the  $1.46-M_{\odot}$  model, and both a reduced and a delayed mass accretion rate along the equatorial direction compared with what would prevail in the absence of rotation. At the end of each simulation, the total neutron star angular momentum is  $1.35 \times 10^{49} \text{ erg s}$  ( $1.13 \times 10^{49} \text{ erg s}$ ) for the  $1.46-M_{\odot}$  model, using the density cut at  $10^{10} \text{ g cm}^{-3}$  ( $10^{11} \text{ g cm}^{-3}$ ), and  $4.57 \times 10^{49} \text{ erg s}$  ( $2.79 \times 10^{49} \text{ erg s}$ ) for the  $1.92-M_{\odot}$  model. However, the accretion rate at a given Eulerian radius is higher and longer-lived at smaller latitudes, because of the larger amount of mass available and the flatter density profile in those regions. Overall, the presence of a massive accretion disk in the fast rotating model complicates the definition of the neutron star mass at such early times. Evolution over minutes/hours/days will likely lead to significant accretion onto the neutron star, resulting in a much higher final mass.

The final rotational to gravitational energy ratio  $T/|W|$  is 0.059 for the  $1.46-M_{\odot}$  model and 0.262 for the  $1.92-M_{\odot}$  model. These values are large and for the latter model, large enough to cause the growth of secular and perhaps even dynamical instabilities (Tassoul 2000). Using realistic post-bounce configurations for a rotating massive star progenitor, Ott et al. (2005a) find a dynamically unstable spiral mode for  $T/|W|$  as low as  $\sim 0.08$ . Thus, it is likely that the PNS structures found here, especially for the  $1.92-M_{\odot}$  model, would develop some non-axisymmetric instability that would cause, among other things, outward angular momentum transport.

These results are significantly different from those of Fryer et al. (1999), who obtained a successful explosion

$\lesssim 100$  ms after bounce, a PNS mass of  $\sim 1.2 M_{\odot}$ , and a  $\sim 1$  s period at  $\sim 200$  ms after core bounce. Such different conclusions stem from their adoption of slow, solid-body progenitor rotation, with most of the angular momentum stored in the outer mantle and blown away by the explosion, rather than being accreted by the PNS.

## 6. NEUTRINO SIGNATURES

The first observational signature of an AIC explosion would be the copious emission of neutrinos immediately after core bounce. As discussed above, the properties of the bounce of the core and the nascent neutron star are close enough to those obtained in simulations of the core collapse of massive progenitors that one expects a neutrino signal with a somewhat similar evolution and character (see, for example, the predictions for the  $11.0-M_{\odot}$  model of Woosley & Weaver 1995 in Dessart et al. 2005).

In Fig. 9, we show the neutrino luminosities (on a log scale) for the  $1.46-M_{\odot}$  (left panel) and  $1.92-M_{\odot}$  (right panel) models, with distinct curves for the different neutrino flavors (solid line:  $\nu_e$ ; dashed line:  $\bar{\nu}_e$ ; dash-dotted line: “ $\nu_{\mu}$ ”), as well as different colors for the equatorial (black) and polar (red) directions. These are luminosities in the sense that the flux in each direction is scaled by  $4\pi R^2$  where  $R$  is a spherical radius, of 250 km for the  $1.46-M_{\odot}$  model and 400 km for the  $1.92-M_{\odot}$  model (chosen to be well above the neutrinosphere for the energy at the peak of the neutrino distribution). They correspond to the total luminosity that would have obtained had the selected directional flux been the same in all directions. The temporal evolution of the various fluxes for both models is comparable. The total neutrino luminosity reaches a maximum of  $5.2 \times 10^{53} \text{ erg s}^{-1}$ , mostly due to the  $\nu_e$  neutrino contribution, and decreases to  $\sim 4 \times 10^{52} \text{ erg s}^{-1}$  at 500 ms after bounce in the  $1.46-M_{\odot}$  model, with a further 30% decrease for the  $1.92-M_{\odot}$  model. At later times, the main reason for this difference is the much lower “ $\nu_{\mu}$ ” neutrino luminosity in the  $1.92-M_{\odot}$  model. This reduction has been seen and discussed by Fryer & Heger (2000) in the context of the collapse of rotating cores of massive progenitors. The smaller core densities (weaker bounce) achieved in models with fast rotation lead to smaller temperatures and, consequently, smaller neutrino emission, with a larger effect for the  $\nu_{\mu}$  and  $\nu_{\tau}$  neutrinos (grouped under the name “ $\nu_{\mu}$ ” here). So, while the globally lower neutron star densities in the fast-rotating model induce a reduction in neutrino luminosity compared to the  $1.46-M_{\odot}$  model, the same effect introduces a latitudinal variation of neutrino fluxes in the faster rotating model, with fluxes, irrespective of neutrino flavor, larger by a factor of about two along the pole than along the equator (note that at a radius of 250 km, the difference is higher and on the order of three). This variation, not discussed by Fryer & Heger (2000), results from the further variation of the neutrinosphere temperatures with latitude within a given rotating model. In both models, but more so in the  $1.92-M_{\odot}$  model, the temperature gradient and the temperatures are reduced at the neutrinosphere (for a given energy group) along the equator compared to the poles, irrespective of energy group and flavor, as is clearly visible in Fig. 10. For example, we see that the temperature on the  $10^{10} \text{ g cm}^{-3}$  contour is 4 MeV in the

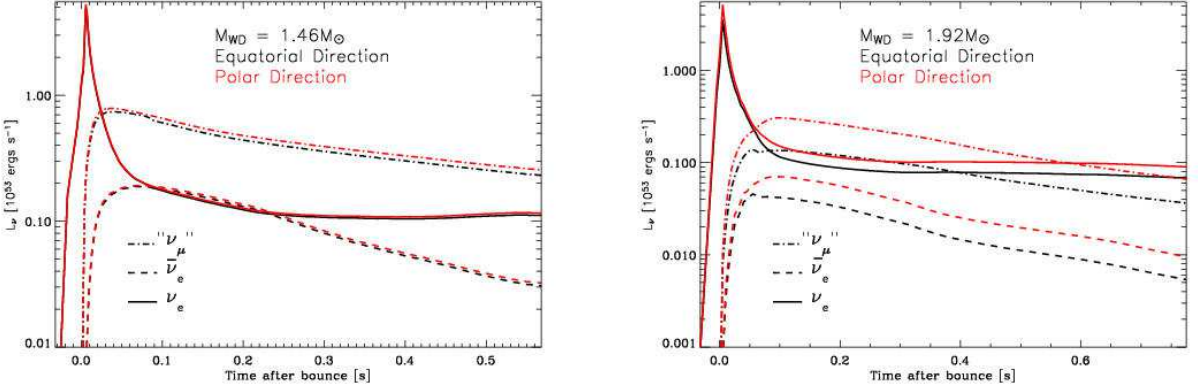


FIG. 9.— Flavor- and angle-dependent neutrino luminosities for the  $1.46\text{-M}_\odot$  (left) and  $1.92\text{-M}_\odot$  (right) progenitors, for an adopted radius of  $R = 250$  km for the former and  $R = 400$  km for the latter. Luminosities shown as solid, dash-dotted, and dashed lines correspond to  $\int_{d\Omega} d\Omega R^2 F_\nu(R, \theta, \varepsilon_\nu)$  for the  $\nu_e$ ,  $\bar{\nu}_e$ , and “ $\nu_\mu$ ” neutrinos, respectively, and in black for the equatorial direction ( $\theta = \pi/2$ ) and in red for the polar direction ( $\theta = 0$ ). Of particular relevance to the asymptotic electron fraction of the ejecta is the higher electron-neutrino luminosity compared to that of the anti-electron neutrinos, by a factor of at least ten in the  $1.92\text{-M}_\odot$  model (right). Note that the vertical scale extends down to  $10^{51}$   $\text{erg s}^{-1}$  for the  $1.46\text{-M}_\odot$  model and to  $10^{50}$   $\text{erg s}^{-1}$  for the  $1.92\text{-M}_\odot$  model.

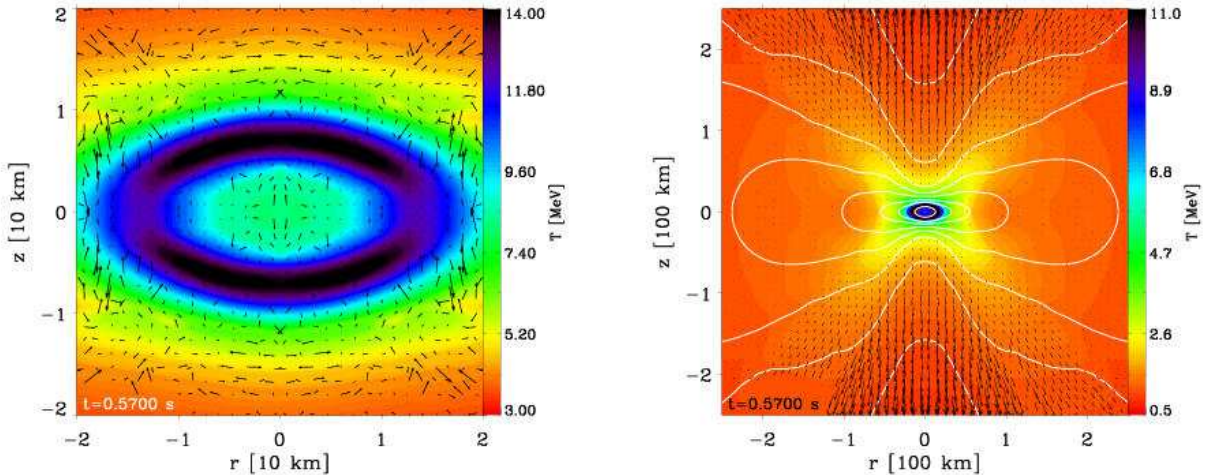


FIG. 10.— Color map of the matter temperature for the  $1.92\text{-M}_\odot$  model at the last snapshot. We overplot the contours of the density every decade, starting with  $10^{14} \text{ g cm}^{-3}$  for the innermost line. *Left*: View of the innermost region ( $\sim 20$  km), showing the latitudinal variation of the temperature even on the innermost density contour. The velocity field reveals the presence of fluid motions along cylinders due to rotation (see §7), thereby preventing convection. A ten-fold magnification of the velocity-vector length, saturated at a value of  $9130 \text{ km s}^{-1}$ , has been applied to better render the fluid motions. *Right*: Zoom out of the left slide, showing the large temperature variation along the  $10^{10-11} \text{ g cm}^{-3}$  density contour, which corresponds reasonably well to the neutrinosphere location at the peak of the neutrino energy distribution (see Fig. 8). The vector of maximum length corresponds to a velocity magnitude of  $11300 \text{ km s}^{-1}$ .

polar direction and 0.5 MeV in the equatorial direction. Within the neutrinosphere region, we find fluid velocities that are oriented preferentially in the  $z$ -direction, along cylinders, illustrating the weak or absent convection that results from the stabilizing specific angular momentum profile (Fryer & Heger 2000; Heger et al. 2000; Ott et al. 2005b; see also §7). Along a given angular slice, the temperature has a maximum at mid-latitudes, caused by enhanced ( $\nu_e$ ) neutrino energy deposition in this direction. These regions offer a tradeoff, since the flux is still higher at such latitudes than along the equator, while the density is relatively higher than along the poles (see §8). The latitudinal variations seen in the collapsed models of AIC progenitors are extreme, and, indeed, for the

slower rotation rates typically obtained for massive-star core-collapse progenitors (Heger et al. 2000), a modest anisotropy is found instead (Walder et al. 2005).

We document further the neutrino signatures of the AIC of white dwarfs by showing in the top row of Fig. 11, for the  $1.46\text{-M}_\odot$  (left) and  $1.92\text{-M}_\odot$  (right) models, the time-integrated neutrino emission at infinity for each flavor, as a function of neutrino energy. In the bottom three panels of each column, we show the individual neutrino distributions at three representative times of the simulations (at bounce, halfway through the simulation, and at the last simulated time). The overall flux level and hardness of the energy distribution are higher along the polar direction, the variation at a given time towards

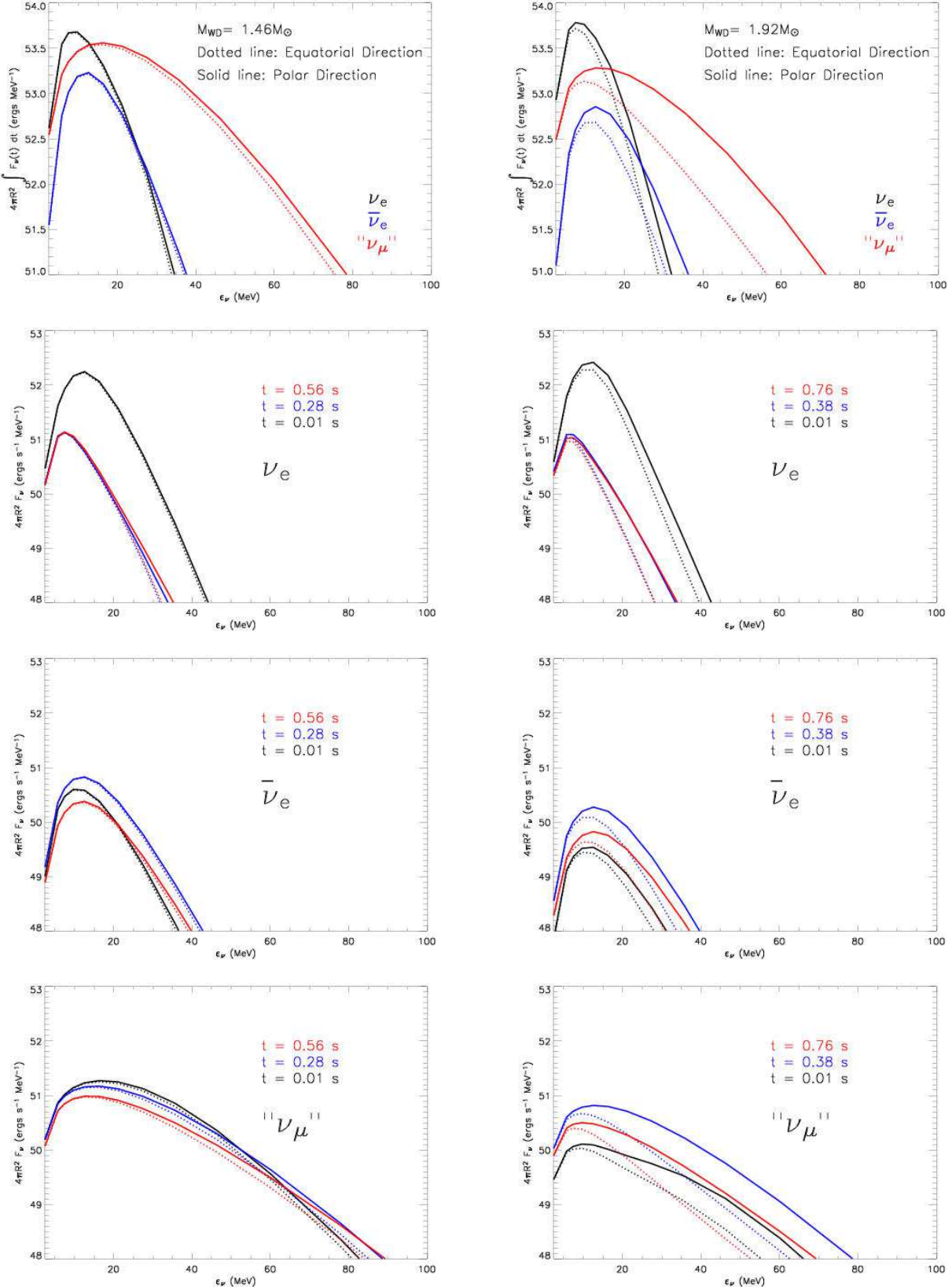


FIG. 11.— *Top Left:* Time integral, until 570 ms after bounce, of the neutrino luminosity, set equal to  $\int_{\Omega} R^2 F_{\nu}(R, \theta) d\Omega$  ( $\theta$  is the polar angle,  $R$  is spherical radius, and  $\Omega$  is the solid angle; see §6), at  $R = 250$  km, for each neutrino flavor (black:  $\nu_e$ ; blue:  $\bar{\nu}_e$ ; red: “ $\nu_{\mu}^{\prime\prime}$ ”), and along the polar (solid line) and equatorial (dotted line) directions. *Bottom left panels:* Neutrino energy distribution, for each neutrino flavor, at 10 ms (black), 280 ms (blue), and 560 ms (red) post-bounce times, for both equatorial (dotted) and polar (solid) directions. *Right column:* Same as left column, but this time for the  $1.92 M_{\odot}$  model, using a radius  $R = 600$  km. In the bottom three panels, the times selected are now 10 ms (black), 380 ms (blue), and 760 ms (red) after bounce. Note the much larger contrast between the equatorial and polar fluxes and energy distributions.

higher latitude mimicking the time evolution seen for non-rotating core collapse simulations of massive star progenitors. We compute the average neutrino energies, here defined as

$$\sqrt{\langle \varepsilon_\nu^2 \rangle} \equiv \left[ \frac{\int d\varepsilon_\nu \varepsilon_\nu^2 F_\nu(\varepsilon_\nu, R)}{\int d\varepsilon_\nu F_\nu(\varepsilon_\nu, R)} \right]^{\frac{1}{2}}.$$

For the  $1.46\text{-M}_\odot$  model ( $R = 250$  km), we obtain similar values to within 2-3% along the pole and along the equator with  $\langle \varepsilon_{\nu_e} \rangle = 10$  MeV,  $\langle \varepsilon_{\bar{\nu}_e} \rangle = 15$  MeV, and  $\langle \varepsilon_{\nu_\mu} \rangle = 24$  MeV. For the  $1.92\text{-M}_\odot$  model ( $R = 600$  km), we obtain systematically lower values than for the  $1.46\text{-M}_\odot$  model, and for lower latitudes. Along the equator (pole), we obtain  $\langle \varepsilon_{\nu_e} \rangle = 9$  MeV (10 MeV),  $\langle \varepsilon_{\bar{\nu}_e} \rangle = 14$  MeV (16 MeV), and  $\langle \varepsilon_{\nu_\mu} \rangle = 16$  MeV (21 MeV). Note that this definition of the neutrino “average” energy is similar to that found in Thompson et al. (2003), who used the mean intensity  $J_\nu$  in place of the flux  $F_\nu$ . Since we are close to free-streaming regimes at the adopted radii for the peak of the neutrino energy distribution, the two are equivalent.

In the  $1.46\text{-M}_\odot$  model, and at late times, we see that the neutrino display is more dramatic (total flux is twice as high) and is characterised by a harder spectrum than in the  $1.92\text{-M}_\odot$  model. This is due to the more compact and, thus, hotter neutrinospheres of the neutron star formed by the lower-mass white dwarf progenitor.

## 7. ROTATION AND THE REMNANT DISK

Let us now turn our discussion to the angular momentum and angular velocity budget and profiles in our simulations. As discussed in §§4–5, we find that the early neutron stars have comparable masses in the two simulations, the rest residing not so much in the outflow than in a substantial amount of “circum-neutron star” disk material, rotating fast, but having little outflow or inflow velocity (see Fig. 6).

In Fig. 12, we plot a temporal sequence of the equatorial radial profile of the angular velocity (top row) and specific angular momentum (bottom row), for the  $1.46\text{-M}_\odot$  model (left column) and  $1.92\text{-M}_\odot$  model (right column). In the  $1.46\text{-M}_\odot$  model, the central angular velocity is  $\sim 0.1 \text{ rad s}^{-1}$  (or a period  $P = 63$  s) at the start of the simulation (initial conditions in the YL05 progenitor), and  $\sim 1000 \text{ rad s}^{-1}$  ( $P = 6.3$  ms) at the end the simulation, a spin-up factor of 10000. In the  $1.92\text{-M}_\odot$  model, we start with a much higher angular rotation rate of  $\sim 20 \text{ rad s}^{-1}$  ( $P = 0.3$  s), but the final values are comparable with those of the  $1.46\text{-M}_\odot$  model, being  $\sim 2800 \text{ rad s}^{-1}$  ( $P = 2.2$  ms). Thus, both simulations lead to the formation of a neutron star with a period of a few milliseconds, although we expect the neutron star formed in the  $1.92\text{-M}_\odot$  model to further accrete mass and angular momentum, which may spin-up the residue to even shorter periods. The general angular velocity and specific angular momentum profiles for both models are quite similar. Despite wiggles observed in the  $1.46\text{-M}_\odot$  model in the inner 10 kilometers (which we associate with slight numerical artifacts along the axis - this problem is not present in the  $1.92\text{-M}_\odot$  model, whose grid covers only  $90^\circ$ ), the neutron star is close to solid-body rotation out to 30 km, showing a steady and smooth decline with radius beyond. In all four panels, we overplot as a broken and black line the corresponding local Keplerian angular velocity,

$\Omega_{\text{Keplerian}}(r) = \sqrt{GM/r^3}$ , where  $G$  is the gravitational constant and  $M$  is the mass interior to the radius (cylindrical, or spherical). (For these plots, we employ the corresponding neutron star mass.) The angular velocity or specific angular momentum profiles beyond 30 km graze the corresponding line for the Keplerian value, being always lower by a few tens of percent. In the  $1.46\text{-M}_\odot$  model, the profiles evolve significantly toward this Keplerian limit, angular momentum being gained along the equatorial direction through the radial infall of non-zero latitude material. The constancy of the angular velocity with  $z$  allows a significant gain from such infall. In the  $1.92\text{-M}_\odot$  model, the rotational properties along the equator are originally closer to the Keplerian values, but, accordingly, evolve little. In both models, angular momentum is transported outwards, first in material blown away by the shock wave initiated at core bounce, and then in the neutrino-driven wind. This occurs as the outflowing material wraps around the progenitor white dwarf and eventually meets along the equator. There is no “physical” viscosity in the code that would permit a proper modeling of the accretion disk. Mass accretion should occur in partnership with outward transport of angular momentum over a longer timescale, yet to be determined.

In the  $1.92\text{-M}_\odot$  model, at the end of the simulation, the near-Keplerian disk extends from 30 km out to  $\sim 1800$  km, covering a range of densities (temperatures) from  $10^{13} \text{ g cm}^{-3}$  down to  $10^8 \text{ g cm}^{-3}$  (3 MeV down to 0.1 MeV; Fig. 5).

## 8. ENERGETICS AND THE NEUTRINO-DRIVEN WIND

Given that it leads to the formation of a  $\sim 1.4\text{-M}_\odot$  neutron star, the AIC of a  $1.4\text{-}2.0\text{-M}_\odot$  white dwarf is expected to result, in the case of a successful explosion, to an outflow of modest mass. Furthermore, due to the similarity with the core collapse of massive star progenitors, their explosion kinetic energy should be lower than the  $\sim 10^{51}$  erg inferred, e.g., for SN1987A (Arnett 1987).

As discussed in §4 and §7, the total sum of the neutron star and disk masses is very close to the original progenitor mass, leaving typically a few  $0.001\text{-M}_\odot$  for the ejected material. Integrating all the mass that has left the grid over the course of the simulation, as well as all the material outflowing with a positive radial velocity greater than  $10000 \text{ km s}^{-1}$  (which is of the order of the escape velocity at a radius of 3000 km) we find a value of  $4 \times 10^{-3} \text{ M}_\odot$  for the  $1.46\text{-M}_\odot$  model and  $3 \times 10^{-3} \text{ M}_\odot$  for the  $1.92\text{-M}_\odot$  model. In Fig. 14, we show the evolution of the corresponding gravitational (blue), thermal (cyan), and kinetic (2D planar: red; rotational: green) energies for this outflowing material as solid lines, including the total energy as a black dotted line. At the last computed time, the total energy is indeed lower than that inferred for standard core collapse. Adopting a radial velocity cut of  $10000 \text{ km s}^{-1}$ , we find an energy at the last simulated time of  $2.7 \times 10^{49}$  erg for the  $1.46\text{-M}_\odot$  model and  $2 \times 10^{49}$  erg for the  $1.92\text{-M}_\odot$  model. Note that energy is still being pumped into the wind by the slowly decaying neutrino luminosity emanating from the neutron star; the trend of the total energy curve suggests that the total energy of the explosion will be 2-3 times higher, thus  $\sim 10^{50}$  erg for the  $1.46\text{-M}_\odot$  model and  $\sim 5 \times 10^{49}$  erg for the

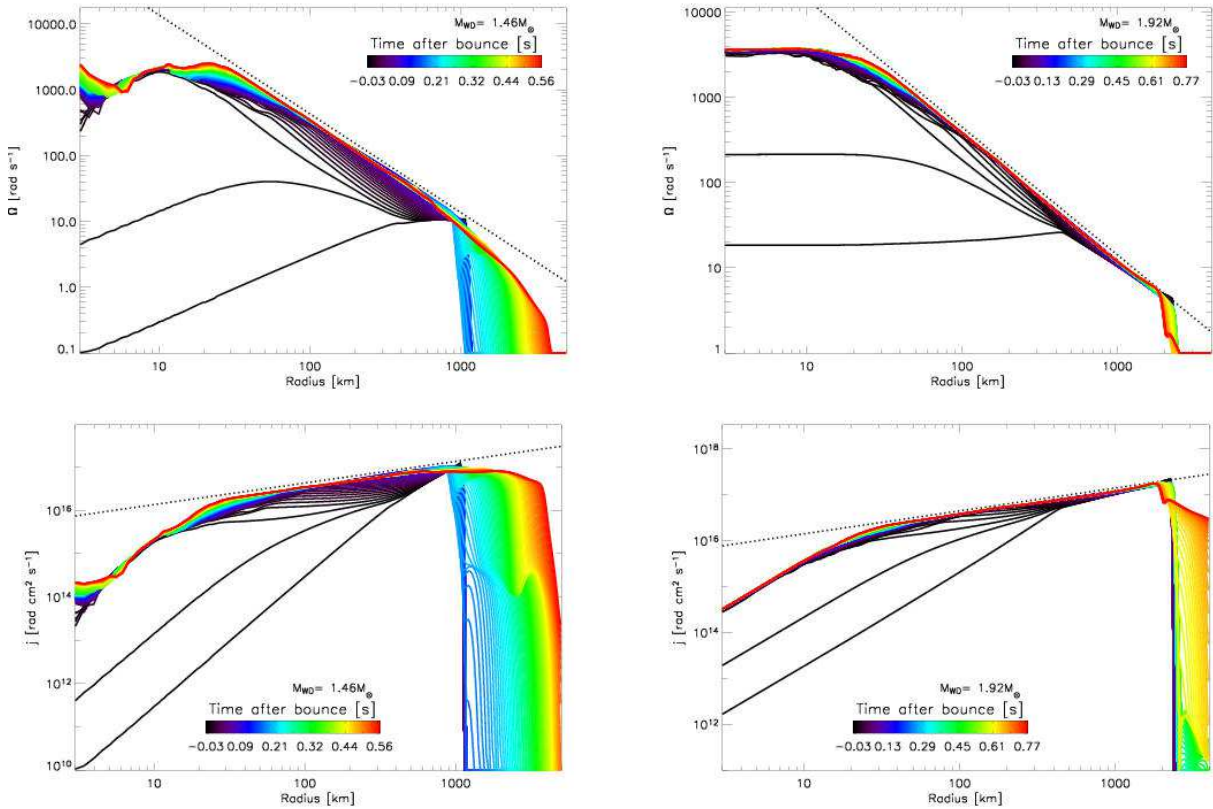


FIG. 12.— *Top:* Time evolution of the equatorial angular velocity profile for the  $1.46M_{\odot}$  (left) and  $1.92M_{\odot}$  (right) progenitor models. *Bottom:* Same as above, but this time for the specific angular momentum  $j$ . Note its outward increase, which acts as a stabilizing influence on convective instabilities (Heger et al. 2000), as well as the rise, from zero, to larger values after  $\sim 200$  ms as the neutrino-driven wind wraps around the white dwarf and brings rotating material to low latitudes. For all panels, we overplot as a dotted black line the corresponding Keplerian value, i.e.,  $\Omega_{\text{Keplerian}}(r) = \sqrt{GM/r^3}$ . See text for details.

### 1.92-M<sub>⊙</sub> model.

This is over one order of magnitude smaller than the explosion energy inferred for normal core-collapse supernovae. The AIC of white dwarfs is likely to lead generically to underenergetic explosions because there is too little mass to absorb neutrinos, most of it being quickly accreted while the rest is centrifugally-supported at large radii, far beyond the region where there is a positive net gain of electron-neutrino energy. Interestingly, similar underenergetic explosions are obtained by Kitaura et al. (2005) and Buras et al. (2005b) for initial main sequence stars of  $8.8M_{\odot}$  (Nomoto 1984, 1987) and  $11.2M_{\odot}$  (Woosley, Heger, & Weaver 2002). Echoing the properties of AIC progenitors, the low envelope mass and fast declining density (and, therefore, accretion rate) are key beneficial components for the success of neutrino-driven explosions, but the same properties are also why the explosion is necessarily underenergetic.

The various curves also show a few dips and bumps. The first bump, most pronounced in the  $1.92M_{\odot}$  model, is associated with an early outflow that eventually fell back to smaller radii, while subsequent bumps are caused by episodic mass loading of the neutrino-driven wind, which sets in  $\sim 200$  ms after core bounce and drives a  $8 \times 10^{-3} M_{\odot} \text{ s}^{-1}$  ( $5 \times 10^{-3} M_{\odot} \text{ s}^{-1}$ ) mass loss rate in the  $1.46M_{\odot}$  ( $1.92M_{\odot}$ ; see also Fig. 15, top panel) model. The higher-mass flux in the  $1.46M_{\odot}$  model results from the higher neutrino luminosity, higher mean neutrino

energies, and bigger opening angle of escape for the neutrino-driven wind. Interestingly, this mass flux is strongly angle-dependent, varying by a factor of a few between the pole and the angle that grazes the pole-facing side of the disk. As described in §4, the dynamical effects of the neutrino-driven wind are to entrain the material lying along this interface, tearing the disk via Kelvin-Helmholtz shear instabilities and mass-loading the wind along the corresponding latitudes. Further in, neither this wind nor the neutrinos have an appreciable dynamical impact in driving the disk material outwards, a feature only exacerbated by the reduced neutrino flux at low latitudes. In Fig. 15, we show in the bottom panel the latitudinal variation of the asymptotic velocity (solid line) and the density (dotted line). Both show an overall decrease towards lower latitudes by a factor of three. The dip in density and higher values of the velocity along the pole to around  $70^{\circ}$  latitude are possibly due to wind mass loading, in combination with centrifugal support at the neutrinosphere for off-polar latitudes. In Fig. 16, we show at early times (top row) and at the last simulated time (bottom row) for the  $1.46M_{\odot}$  model (left column) and the  $1.92M_{\odot}$  model (right column) color maps of the total neutrino flux in the radial direction, with isodensity contours overplotted as white curves, and velocity vectors as black arrows. First, due to the history of the collapse, the neutron star is relatively devoid of overlying material in the polar direction, while for the higher-mass

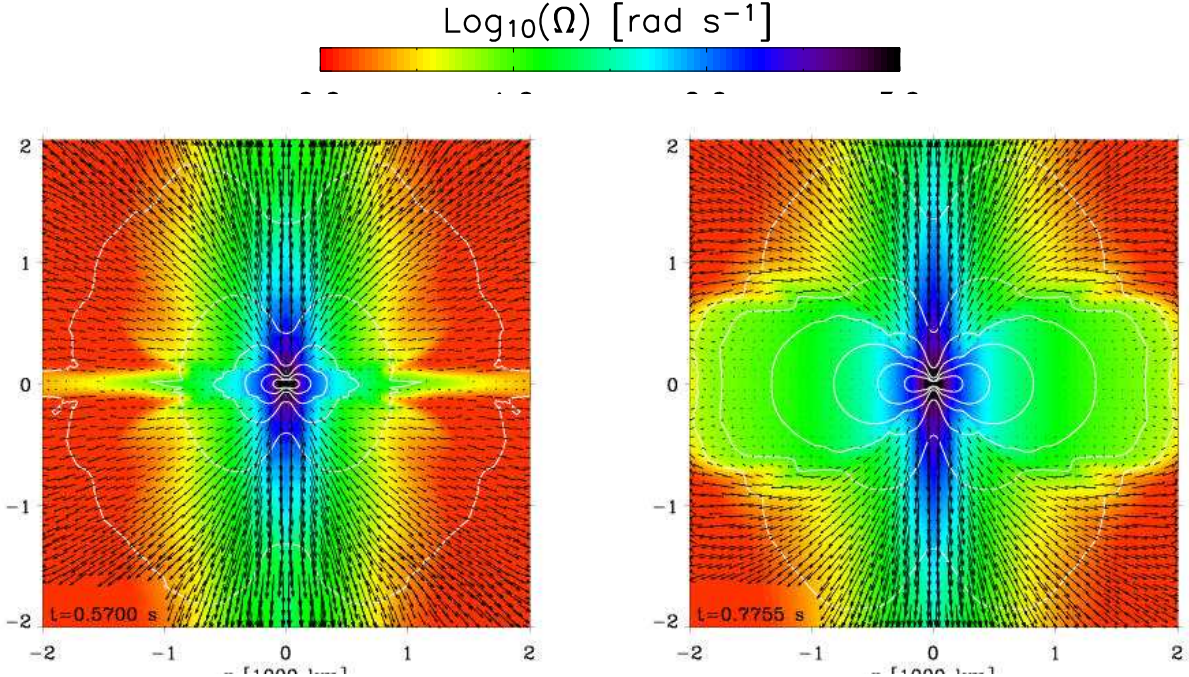


FIG. 13.— Color map of the logarithm of the angular velocity, at the last simulated time (570 ms for the  $1.46\text{-M}_\odot$  model, and 775 ms for the  $1.92\text{-M}_\odot$  model), out to a maximum radius of 2000 km, for the  $1.46\text{-M}_\odot$  (left) and  $1.92\text{-M}_\odot$  (right) progenitors. The initial angular velocity profiles  $\Omega(r, z)$ , functions of the cylindrical radial coordinate only (YL05), are given for the equatorial direction in Fig. 12 (bottom curve). To enhance the visibility, we have reduced the colorbar range (see Fig. 12 for the unsaturated values). We also overplot in white the corresponding contours of the density for every decade between  $10^4$  and  $10^{10} \text{ g cm}^{-3}$ . The vector of maximum length corresponds to a velocity magnitude of  $29000 \text{ km s}^{-1}$  (outflow) in both panels. The spatial scale is 4000 km in width.

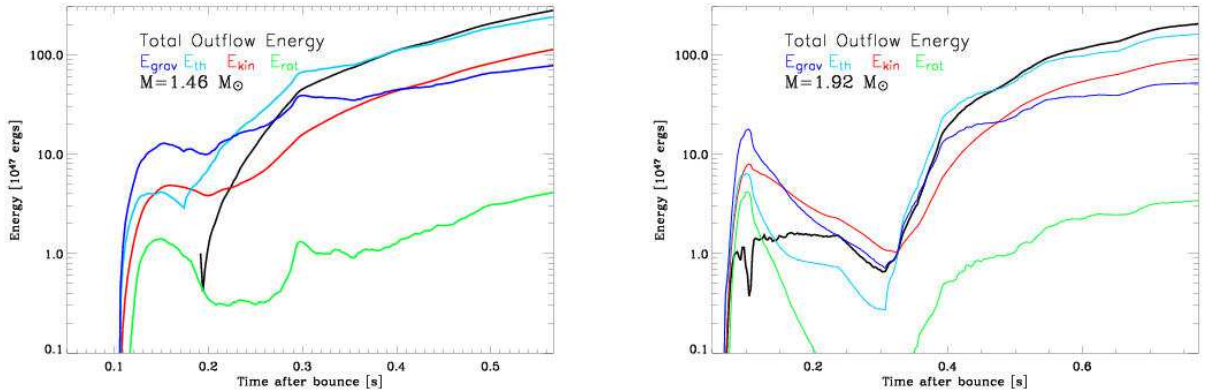


FIG. 14.— Time evolution of outflow gravitational (blue), thermal (cyan),  $(r, z)$ -kinetic energy (red), and rotational (green) energy (on a log scale) for the  $1.46\text{-M}_\odot$  model (left) and  $1.92\text{-M}_\odot$  model (right), accounting for all the material with radial outflow velocity higher than  $10000 \text{ km s}^{-1}$ . The explosion energy at the end of the simulation is  $2.7 \times 10^{49} \text{ erg}$  for the  $1.46\text{-M}_\odot$  model and  $2 \times 10^{49} \text{ erg}$  for the  $1.92\text{-M}_\odot$  model, with final expected energies of  $\sim 10^{50} \text{ erg}$  and  $\sim 5 \times 10^{49} \text{ erg}$ , in the same order. See text for details.

progenitor a massive ( $\sim 0.6 \text{ M}_\odot$ ), dense ( $10^{6-10} \text{ g cm}^{-3}$ ), near-Keplerian disk obstructs the neutron star at latitudes  $\lesssim \pm 40^\circ$ . Given this configuration, conditioned essentially by the mass distribution of the progenitor white dwarf, the dynamical effect of a spherically-symmetric neutrino flux would be enhanced along the “excavated” polar direction. Indeed, we see a strong neutrino-driven wind in the polar direction that does not exist in directions within  $\sim \pm 40^\circ$  of the equator. However, even in the absence of this anisotropic matter distribution,

Fig. 16 reveals the strong latitudinal variation of the neutrino flux at a given Eulerian radius, a variation that is established independently of the configuration of the circum-neutron star disk material. What controls the flux geometry is the combination of two effects. First, the exceptional elongation of the neutrinospheres along the equatorial direction leads to a decoupling radius (surface) about 10 (100) times bigger for a polar observer than for an equatorial observer. The angle-dependent decoupling radius of neutrinos mitigates this result (Walder

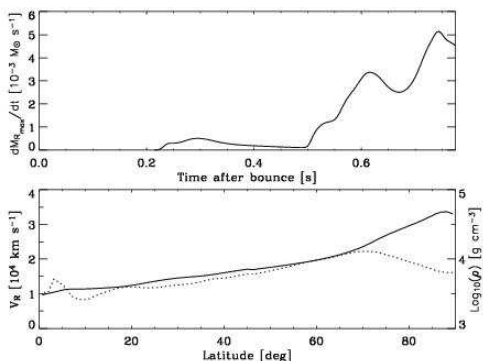


FIG. 15.— *Top:* Time evolution of the total mass loss rate through the outer grid radius,  $dM_{R_{\max}}/dt$ , in the  $1.92\text{-}M_{\odot}$  model. *Bottom:* Latitudinal dependence of the radial velocity (solid line) and density (broken line) in the  $1.92\text{-}M_{\odot}$  model *at the latest time* computed, when the neutrino-driven wind has reached a steady-state.

et al. 2005), but, as shown in Fig. 16, the latitudinal variation along different directions persists in the total neutrino flux. Similarly, Fig. 17 shows the anisotropy of the  $\nu_e$  neutrino flux, rendered by the corresponding flux vectors. Notice how the base of the flux vectors in the high-density central regions is perpendicular to the local isodensity (or, equivalently, equipotential) contour. Second, as shown in Fig. 10, the temperature and its radial-gradient along a given isodensity contour are both significantly lower along the equatorial direction, leading to reduced diffusive fluxes. These properties are reminiscent of the effect of gravity darkening (von Zeipel 1924) in fast rotating (non-compact) stars and the associated scaling of the radiative flux with the local effective gravity (see Owocki et al. 1996), although this may be the first time it is reported in the context of a protoneutron star (but see Walder et al. 2005). With such a polar-enhanced wind, the angular momentum loss rate is reduced, with consequences for the spin evolution of the PNS.

#### 9. EJECTA COMPOSITION

In Fig. 18, we show for the two baseline models the electron fraction ( $Y_e$ ) distribution of the material in the ejecta (material outside the neutron star moving outwards with a radial velocity greater than  $10000\text{ km s}^{-1}$ ), accounting as well for the mass loss through the outer grid radius. Such cumulative outflow amounts to  $4 \times 10^{-3} M_{\odot}$  for the  $1.46\text{-}M_{\odot}$  model and  $3 \times 10^{-3} M_{\odot}$  for the  $1.92\text{-}M_{\odot}$  model. We obtain double-peak profiles, the first blast propelling symmetric material ( $Y_e = 0.5$ ), subsequently followed after 200 ms by progressively neutron-rich material, i.e.,  $Y_e = 0.25\text{--}0.35$ , in the neutrino-driven wind. Note that for these runs we enforced an upper limit of 0.5 to the computed  $Y_e$  values. Fryer et al. (1999) obtained an ejecta mass in the vicinity of  $0.2 M_{\odot}$ , two orders of magnitude larger than our values. Because our ejecta masses are much smaller, we find that the mass loss rates and the kinetic energies associated with the neutrino-driven wind are relatively more important for the global energetics of the AIC of white dwarfs.

At late times, the asymptotic electron fraction  $Y_e^a$  of the neutrino-driven wind varies with latitude (despite the

smooth variation of other quantities at correspondingly larger distances). Material ejected within  $20^{\circ}$  of the pole has an electron fraction of  $\sim 0.5$ , while towards the equator, this electron fraction decreases to 0.3, rising again to near 0.5 values in regions belonging to the disk (see bottom row panels in Fig. 4). The  $Y_e^a$  values seen in our simulations are in fact already set when wind material leaves the vicinity of the neutrinosphere, whose properties depend on the particle trajectory under scrutiny. We know from previous studies (Qian & Woosley 1996; Wheeler et al. 1998; Thompson et al. 2001; Pruet et al. 2005; Frölich et al. 2005) that the asymptotic electron fraction of the ejecta is controlled by competing factors. The electron and anti-electron neutrino luminosities, modulated by the hardness of their respective energy distributions, influence the electron flavor production rates via the reactions  $\nu_e n \rightarrow p e^-$  and  $\bar{\nu}_e p \rightarrow e^+ n$  and, thereby, the neutron-richness of the ejecta. The expansion timescale sets the duration over which interactions between neutrinos and nucleons can take place.

The starting value of the electron fraction, i.e., at the base of the outflow, is altered by the above factors and differs from the asymptotic value seen. In Fig. 19, we show a color map of the electron fraction in the inner 200 km, highlighting the butterfly shape of the deleptonized region in cross section, in stark contrast with the corresponding near-spherical shape seen in core-collapse simulations of both rotating and non-rotating progenitors (Keil et al. 1996; Walder et al. 2005; Dessart et al. 2005). Deleptonization obtains preferentially in the vicinity of the dumbbell-shaped neutrinosphere, and stretches outwards for off-polar latitudes. Along the equator, deleptonization ceases at smaller radii due to the lower effective temperatures (tied to the neutrino fluxes). Temperature and neutrino flux are in fact intertwined, since energy deposition by neutrinos may raise the temperature locally in the so-called gain region. This is also vividly represented in Fig. 19 (right) by the net gain associated with electron-neutrino energy deposition in this inner region, which also shows the same butterfly shape. Electron neutrinos emerge from the neutron star, and, due to the dumbbell neutrinosphere morphology, at much smaller radii along the poles than for off-polar latitudes. The decreasing neutrino flux (dilution) reduces this energy deposition beyond  $\sim 50$  km, and even at smaller radii along the equator due to the additional flux reduction there (Fig. 16).

The asymptotic value of the material electron fraction is determined in the vicinity of the neutrinosphere and, therefore, is directly influenced by this configuration of the inner  $Y_e$  distribution. Along the pole, the wind carries initially low  $Y_e$  material that absorbs electron neutrinos, whose associated luminosity is one magnitude higher than that of the anti-electron neutrinos (see Fig. 9), raising the electron fraction to the ceiling value of 0.5 artificially adopted in these calculations. Away from the pole, the neutrinosphere is located further out, and despite similar neutrinosphere  $Y_e$  values, the larger distance from the neutron star implies a reduced electron-neutrino luminosity and a reduced absorption of neutrinos, leading to asymptotic values of the electron fraction of only  $\sim 0.25$ , not far from the values at the corresponding neutrinosphere. To summarize, the progressive decrease of the electron fraction (and of the entropy) away from the

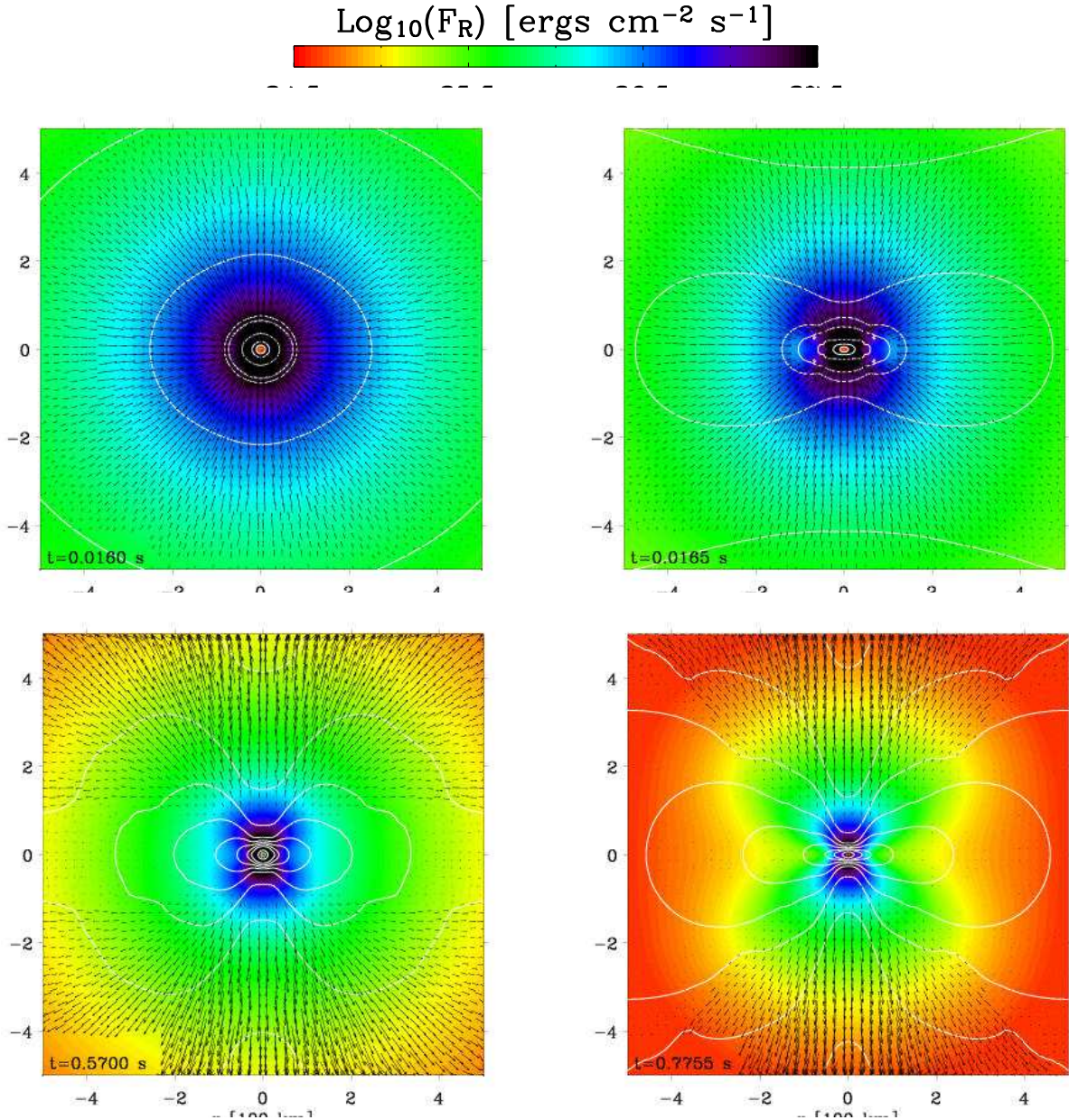


FIG. 16.— Color maps of the total neutrino flux soon after bounce (top row) and at the last simulated time (bottom row), for the  $1.46\text{-M}_\odot$  model (left column) and  $1.92\text{-M}_\odot$  model (right column), with velocity vectors and density contours (for every decade starting from  $10^{14}\text{ g cm}^{-3}$ ). Note the growing flux anisotropy with time, more manifest for the  $1.92\text{-M}_\odot$  model, with regions of high flux coinciding with regions of low density, following primarily the angle-dependent surface area of the neutrinosphere and, secondarily, the latitudinal dependence of the temperature (Fig. 10) near such neutrinospheres. Note the gravity darkening effect *à la von Zeipel*. From top to bottom, left to right, the vector of maximum length corresponds to a velocity magnitude of  $52500\text{ km s}^{-1}$  (infall),  $53000\text{ km s}^{-1}$  (infall),  $18500\text{ km s}^{-1}$  (outflow), and  $15500\text{ km s}^{-1}$  (outflow).

pole is a result of the reduced electron-neutrino luminosities in the vicinity of the latitudinal-dependent neutrinosphere radius (and the associated reduced heating and electron-capture rates).

#### 10. GRAVITATIONAL WAVE SIGNATURE

We estimate the gravitational wave emission from aspherical mass motions in our models via the Newtonian quadrupole formalism as described in Mönchmeier et al.

(1991). In addition, we compute the gravitational wave strain from anisotropic neutrino emission employing the formalism introduced by Epstein (1978) and developed by Burrows & Hayes (1996) and Müller & Janka (1997).

Due to rapid rotation and the resulting oblateness of the core, one would expect that rotating AIC models would have significant gravitational wave signatures. This is true. However, though the contribution to the metric strain in the equatorial plane,  $h_+$ , of the aspher-

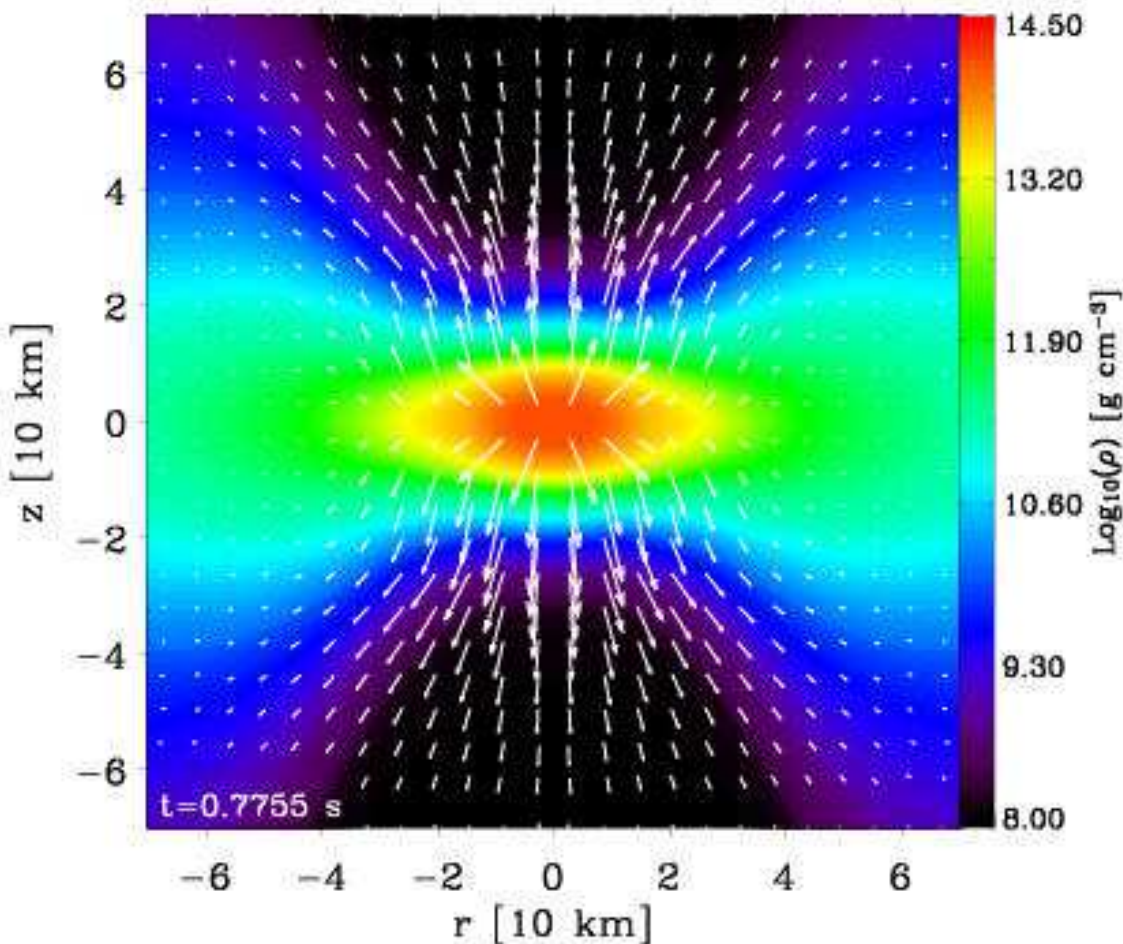


FIG. 17.— Color map of the density, in the inner  $\sim 70$  km, overplotted with white vectors representing the energy-integrated electron-neutrino flux at the last time simulated for the  $1.92\text{-M}_\odot$  model, presented for comparison with the bottom-right panel of Fig. 16. Note how the flux vectors tend to point in a direction perpendicular to the local isochores, modulo variations, e.g., due to the non-uniform temperature distribution, but in general conformity with the von Zeipel theorem which stipulates that the radiative flux should be aligned with the local effective gravity. The vector of maximum length corresponds to a flux magnitude of  $3 \times 10^{37} \text{ erg cm}^{-2} \text{ s}^{-1}$ . For a more quantitative assessment of the electron-neutrino flux magnitude, see Fig. 9 and Fig. 16.

ical and dynamical matter distributions is not small, we find that that of the aspherical neutrino field is larger in magnitude, though at much smaller frequencies. While we calculate that  $h_+(\text{max})$  for the matter in the  $1.46\text{-M}_\odot$  model is  $\sim 5.9 \times 10^{-22}$ , with a spectrum that peaks at  $\sim 430$  Hz, the corresponding  $h_+(\text{max})$  due to neutrinos is  $\sim 4.6 \times 10^{-21}$  (derived from the fluxes at 200 km), but at frequencies between ( $\sim 0.1$ -10 Hz). The total energy radiated in gravitational waves is  $\sim 5.7 \times 10^{-10} \text{ M}_\odot c^2$ . The corresponding numbers for the faster rotating and more massive  $1.92\text{-M}_\odot$  model are  $\sim 3.6 \times 10^{-21}$  (matter),  $\sim 165$  Hz,  $\sim 2.0 \times 10^{-20}$  (neutrinos at 300 km), and  $\sim 7.0 \times 10^{-8} \text{ M}_\odot c^2$ . Note that almost all of the energy is being emitted by mass motions (99.8% in the  $1.46\text{-M}_\odot$  model and 98.4% in the  $1.92\text{-M}_\odot$  model), since the power scales with the time derivative of the wave strain  $h_+$ , which is

small for the waves emitted from the aspherical neutrino field.

We compare the above numbers with those obtained by Fryer, Holz & Hughes (2002) for an AIC model of Fryer et al. (1999) which was setup with a simple, solid-body rotation law and had a final  $T/|W|$  of  $\sim 0.06$  (for our  $1.46\text{-M}_\odot$  model: 0.059; see Table 1). They did not consider anisotropic neutrino emission. Our more realistic initial models yield maximum (matter) gravitational wave strains that are 1.5 to 2 orders of magnitude smaller than those predicted by Fryer, Holz & Hughes (2002). The total energy emissions match within a factor of two since our models emit at higher frequencies.

Based on our results, we surmise that gravitational waves from axisymmetric AIC events may be detected by current LIGO-class detectors if occurring anywhere

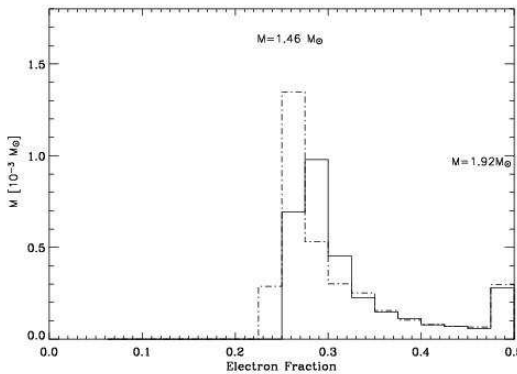


FIG. 18.— Distribution of the total outflow mass (cells with outward radial velocity of at least  $10000 \text{ km s}^{-1}$ ) as a function of electron fraction, taken at the last time for both models (solid line:  $1.92 M_\odot$  model; broken line:  $1.46 M_\odot$  model). The total mass in the outflow, making allowance for any mass lost through the outer grid radius, is  $0.003 M_\odot$  for the  $1.92 M_\odot$  model and  $0.004 M_\odot$  for the  $1.46 M_\odot$  model.

in the Milky Way, but not out to megaparsec distances as suggested by Fryer, Holz & Hughes (2002). It is, however, likely (§5) that at least the  $1.92 M_\odot$  model will undergo a dynamical rotational instability leading to non-axisymmetric deformation (which can not be captured by our 2D approach) and, hence, to copious gravitational wave emission over many rotation periods, greatly enhancing detectability.

## 11. DISCUSSION AND CONCLUSIONS

We have presented a radiation/hydrodynamic study with the code VULCAN/2D of the collapse and post-bounce evolution of massive rotating high-central-density white dwarfs, starting from physically consistent 2D rotational equilibrium configurations (Yoon & Langer 2005). The main results of this study are:

- The AIC of white dwarfs leads to a successful explosion with modest energy  $\lesssim 10^{50} \text{ erg}$ , thus comparable to the energies obtained through the collapse of O/Ne/Mg core of stars with  $\sim 8-11 M_\odot$  main sequence mass (Kitaura et al. 2005; Buras et al. 2005b). This is, however, underenergetic, by a factor of about ten, compared with the inferred value for the core collapse of more massive progenitors leading to Type II Plateau supernovae. Although less and less likely to be the engine behind most core-collapse supernova explosions, the neutrino mechanism can successfully power explosions of low-mass progenitors and AICs due to the limited mantle mass and steeply declining accretion rate.
- Due to high-mass and angular-momentum accretion, white dwarf progenitors leading to AIC can have masses of up to  $\sim 2 M_\odot$  and rotate fast, with rotational to gravitational energy ratios of up to a few percent prior to collapse. The asphericity of such white dwarfs allows the shock generated at core bounce to escape along the poles in just a few tens of milliseconds, opening a hole in the white dwarf along the poles. The blast expands and wraps around the progenitor and escapes the grid ( $\sim 5000 \text{ km}$ ) within a few hundred milliseconds, at which time a neutrino-driven wind has grown in the pole-excavated region of the white dwarf. Both the original blast and the wind show strong latitudinal variations, partly constrained by the obstructing uncollapsed equatorial disk regions of the progenitor, whose centrifugal support prevents it from collapsing on a dynamical timescale. Rotation in such progenitors, thus, affects both directly and indirectly the morphology of the explosion.
- The neutron stars formed have masses on the order of  $1.4 M_\odot$ , with rotation periods close to a millisecond in the rigidly rotating inner  $\sim 30 \text{ km}$ . The final rotational to gravitational energy ratios, for our two test cases, cover 0.06 to 0.26, the latter being large enough to grow non-axisymmetric instabilities. At the end of our simulations, the neutron stars are oblate and pinched along the poles, with polar and equatorial radii in the ratio 1:15 for the faster rotating ( $1.92 M_\odot$ ) model.
- The morphology of the neutron star leads to a latitudinal variation of the neutrino flux, the net energy gain, and the temperature. In the faster rotating model, the “ $\nu_\mu$ ” neutrino flux is reduced, while the anti-electron neutrino flux is a factor of ten lower than that of the electron-neutrino. This raises the electron fraction of the ejected material to values close to 0.5 along the poles, but to only  $\sim 0.25$  at lower latitudes, since the corresponding neutrinosphere is more remote and, thus, the electron-neutrino flux is smaller. This introduces a latitudinal dependence of the electron fraction of the ejected material, but more importantly allows neutron-rich material, with entropy on the order of  $20-40 k_B/\text{baryon}$ , to escape. Thus, a low-entropy r-process might take place under these conditions.
- The high original angular momentum of the progenitor follows the mass and is, thus, found mostly in the neutron star at the end of the simulation. However, rotational energy is also given to the ejecta, which uses it to gain (planar) radial kinetic energy to escape the potential well, while the rest is found in a quasi-Keplerian disk of up to  $0.5 M_\odot$  in the  $1.92 M_\odot$  model. This disk is an essential component of these AICs; it collimates the explosion and the neutrino-driven wind and also suggests a second stage of long-term accretion onto the compact remnant.
- The total ejected mass is only of the order of a few times  $0.001 M_\odot$ , with only a quarter in the form of  $^{56}\text{Ni}$ . The original blast and the short-lived neutrino-driven wind will lead to a considerable brightening of the object, but the small ejecta mass will quickly become optically-thin, gamma rays leaking out rather than depositing their energy to power a durable light curve. Therefore, these explosions should be underluminous and very short lived. Their appearance may also vary considerably with viewing angle, depending on the mass of

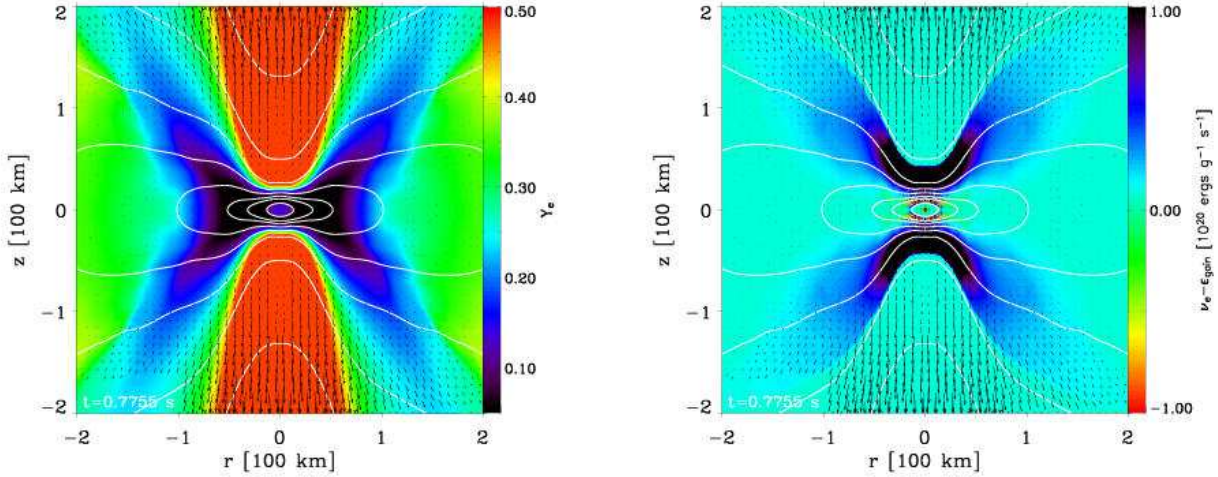


FIG. 19.— *Left:* Color map of the electron fraction in the inner regions of the  $1.92\text{-M}_\odot$  model at the last computed time, with isodensity contours (white lines; every decade, starting at  $10^{14}\text{ g cm}^{-3}$ ) and velocity vectors (black arrows) overplotted, showing in particular the locations of the deleptonized regions and the neutrinospheres. Notice the  $Y_e$  change in the material as it moves away from the neutrinosphere (roughly the  $10^{10-11}\text{ g cm}^{-3}$  contour). It rises steeply from 0.05 to 0.5 in just a few tens of kilometers along the pole, while this rise is more gradual at  $\sim 45^\circ$  latitude, saturating at  $\sim 0.25$ . *Right:* Same as left, but for the net energy gain due to absorption (positive) and emission (negative) of electron neutrinos (the colorbar range used saturates the gain values in the inner regions). Notice how much stronger (and positive) the gain is along the poles, causing the  $Y_e$  of the material to rise steeply to 0.5, while its more modest value away from the pole alters the  $Y_e$  of the corresponding material only up to  $\sim 0.25$ . Note that the anti-electron neutrino flux is one order of magnitude lower than that of the electron neutrinos, and thus, too weak to cause the reverse process of a decrease of the  $Y_e$  of the material. The vector of maximum length corresponds to a velocity magnitude of  $9130\text{ km s}^{-1}$ .

the progenitor and the presence of a sizable disk in the equatorial regions.

This study has shown that more consistent, rotating 2D models alter considerably our understanding of accretion-induced collapse, previously obtained under the simplifying assumptions of spherical symmetry and/or zero rotation. Further improvements will come by including a consistent temperature structure for the progenitor white dwarf and by accounting for the effects of magnetic fields. Due to the rapid differential rotation, magnetic fields could be amplified considerably and result in MHD jets that might alter yet again our overall picture of accretion-induced collapse and the energetics of the phenomenon. Three-dimensional effects may also alter the protoneutron star properties presented here, since the faster rotating ( $1.92\text{-M}_\odot$ ) model is expected to experience non-axisymmetric instabilities.

We acknowledge discussions with and help from Jeremiah Murphy and Casey Meakin. Importantly, we acknowledge support for this work from the Scientific Discovery through Advanced Computing (SciDAC) program of the DOE, grant number DE-FC02-01ER41184 and from the NSF under grant number AST-0504947. E.L. thanks the Israel Science Foundation for support under grant # 805/04, and C.D.O. thanks the Albert-Einstein-Institut for providing CPU time on their Peyote Linux cluster. We thank Jeff Fookson and Neal Lauver of the Steward Computer Support Group for their invaluable help with the local Beowulf cluster. This research used resources of the National Energy Research Scientific Computing Center, which is supported by the Office of Science of the U.S. Department of Energy under Contract No. DE-AC03-76SF00098.

## REFERENCES

Arnett, W.D. 1987, *ApJ*, 319, 136  
 Barkat, Z., Reiss, Y., & Rakavy, G. 1974, *ApJ*, 193, 21  
 Baron, E., Cooperstein, J., & Kahana, J. 1987, *ApJ*, 320, 300  
 Baron, E., Cooperstein, J., Kahana, J., & Nomoto, K. 1987, *ApJ*, 320, 304  
 Belczynski, K., Bulik, T., & Ruiter, A. 2005, *ApJ*, 629, 915  
 Blanc, G., et al. 2004, *A&A*, 423, 881  
 Blinnikov, S.I., Dunina-Barkovskaya, N.G., & Nadyozhin, D.K. 1996, *ApJS*, 106, 171  
 Bruenn, S.W., Raley, E.A., & Mezzacappa, A. 2005, *astro-ph/0404099*  
 Buras, R., Rampp, M., Janka, H.-Th., & Kifonidis, K. 2005a, accepted for publication in *Astron. Astrophys.*, *astro-ph/0507135*  
 Buras, R., Janka, H.-Th., Rampp, M., & Kifonidis, K. 2005b, submitted to *Astron. Astrophys.*, *astro-ph/0512189*  
 Burrows, A., & Hayes, J. 1996, *Physical Review Letters*, 76, 352  
 Burrows, A., Livne, E., Dessart, L., Ott, C., & Murphy, J., 2005, accepted for publication in *ApJ*, *astro-ph/0510687*  
 Dessart, L., Burrows, A., Livne, E., & Ott, C.D. 2005, submitted to *ApJ*, *astro-ph/0510229*  
 Epstein, R. 1978, *ApJ*, 223, 1037  
 Fröhlich, Martnez-Pinedo, G., Liebendörfer, M., Thielemann, F.-K., Bravo, E., Hix, W.R., Langanke, K., & Zinner, N.T. 2005, submitted to *Phys. Rev. Letters*, *astro-ph/0511376*  
 Fryer, C.L., Benz, W., Herant, M., & Colgate, S.A. 1999, *ApJ*, 516, 892  
 Fryer, C.L., & Heger, A. 2000, *ApJ*, 541, 1033  
 Fryer, C. L., Holz, D. E., & Hughes, S. A. 2002, *ApJ*, 565, 430

Greggio, L. 2005, *Astron. Astrophys.*, 441, 1055

Hachisu, I. 1986, *ApJS*, 61, 479

Heger, A., Langer, N., & Woosley, S.E. 2000, *ApJ*, 528, 368

Hillebrandt, W., Nomoto, K., & Wolff, R.G. 1984, *Astron. Astrophys.*, 133, 175

Janka, H.-T., & Mönchmeyer, R. 1989a, *Astron. & Astrophys.*, 209, L5

Janka, H.-T., & Mönchmeyer, R. 1989b, *Astron. & Astrophys.*, 226, 69

Keil, W., Janka, H.-T., & Müller 1996, *ApJ*, 473, 111

Kitaura, F.S., Janka, H.-T., Hillebrandt, W. 2005, submitted to *Astron. Astrophys.*, astro-ph/0512065

Liu, Y. & Lindblom, L. 2001, *MNRAS*, 324, 1063

Livio, M., Buchler, J.R., & Colgate, S.A. 1980, *ApJ*, 238, L139

Livne, E. 1993, *ApJ*, 412, 634

Livne, E., Burrows, A., Walder, R., Thompson, T.A., & Lichtenstadt, I. 2004, *ApJ*, 609, 277

Madau, P., Della Valle, M., & Panagia, N. 1998, *MNRAS*, 297, L17

Mannucci, F., della Valle, M., Panagia, N., Cappellaro, E., Cresci, G., Maiolino, R., Petrosian, A., Turatto, M. 2005, *Astron. Astrophys.*, 433, 807

Mayle, R. & Wilson, J. R. 1988, *ApJ*, 334, 909

Miyaji, S., & Nomoto, K. 1987, *ApJ*, 318, 307

Mochkovitch, R., & Livio, M. 1989, *Astron. Astrophys.*, 209, 111

Mönchmeyer, R., Schaefer, G., Müller, E., & Kates, R. E. 1991, *Astron. Astrophys.*, 246, 417

Müller, E., & Janka, H.-T. 1997, *Astorn. Astrophys.*, 317, 140

Nomoto, K. 1984, *ApJ*, 277, 791

Nomoto, K. 1987, *ApJ*, 322, 206

Nomoto, K., & Kondo, Y. 1991, *ApJ*, 367, L19

Ostriker, J.P., & Mark, J.W.-K. 1968, *ApJ*, 151, 1075

Ott, C.D., Burrows, A., Livne, E., & Walder, R. 2004, *ApJ*, 600, 834

Ott, C.D., Ou, S., Tohline, J.E., & Burrows, A., 2005a, *ApJ*, 625, L119

Ott, C.D., Burrows, A., Dessart, L. & Livne, E. 2006, in preparation

Ott, C.D., Burrows, A., Thompson, T.A., & Livne, E. 2005b, accepted to *ApJ*, astro-ph/0508462

Owocki, S.P., Cranmer, S.R., & Gayley, K.G. 1996, *ApJ*, 472, 115O

Pruet, J., Woosley, S.E., Buras, R., Janka, H.-T., & Hoffman, R. D. 2005, *ApJ*, 623, 325

Qian, Y.-Z., & Woosley, S.E. 1996, *ApJ*, 471, 331

Scannapieco, E., Bildsten, L. 2005, *ApJ*, 629, 85

Shen, H., Toki, H., Oyamatsu, K., & Sumiyoshi, K. 1998, *Nucl. Phys. A*, 637, 43

Swesty, F.D., & Myra, E.S. 2005, astro-ph/0506178

Tassoul, J.-L. 2000, *Stellar Rotation* (Cambridge Univ. Press)

Thompson, T.A., Burrows, A., & Meyer, B.S. 2001, *ApJ*, 562, 887

Thompson, T.A., Burrows, A., & Pinto, P.A. 2003, *ApJ*, 592, 434

von Zeipel, H. 1924, *MNRAS*, 84, 665

Walder, R., Burrows, A., Ott, C.D., Livne, E., Lichtenstadt, I., & Jarrah, M. 2005, *ApJ*, 626, 317

Wheeler, J.C., Cowan, J.J., & Hillebrandt, W. 1998, *ApJ*, 493, L101

Woosley, S.E., & Baron, E. 1992, *ApJ*, 391, 228

Woosley, S.E. & Weaver, T.A. 1995, *ApJS*, 101, 181

Woosley, S.E., Heger, A., & Weaver, T.A. 2002, *Reviews of Modern Physics*, 74, 1015

Yoon, S.-C., & Langer, N. 2004, *Astron. Astrophys.*, 419, 623

Yoon, S.-C., & Langer, N. 2005, *Astron. Astrophys.*, 435, 967

Yungelson, L.R., & Livio, M. 1998, *ApJ*, 497, 168

Yungelson, L.R., & Livio, M. 2000, *ApJ*, 528, 108